Editors' Suggestion

Large eddy simulation of transitional channel flow using a machine learning classifier to distinguish laminar and turbulent regions

Ghanesh Narasimhan, Charles Meneveau, and Tamer A. Zaki
Department of Mechanical Engineering, Johns Hopkins University, Baltimore, Maryland 21218, USA

(Received 7 December 2020; accepted 15 June 2021; published 19 July 2021)

While wall modeling enables significant reduction in computational cost compared to wall-resolved large eddy simulations (LESs), it often fails to capture laminar-to-turbulence transition processes realistically. This issue arises in part because wall models typically assume that the near-wall flow is in a statistically quasiequilibrium turbulent state and hence incorrectly prescribe turbulent wall stresses in regions that are still laminar during transition. In this work we propose an approach in which the application of the wall model is retained within the turbulent regions of transitional flow where even nascent spots exhibit high-Reynolds-number characteristics, but the wall model is not applied in laminar regions. The local distinction between turbulent and laminar regions is performed using a self-organized map (SOM) [see Z. Wu *et al.*, Phys. Rev. Fluids **4**, 023902 (2019)], an unsupervised machine learning classifier. We demonstrate the capability of wall-modeled LES with SOM-based turbulent/nonturbulent classification (WMSOM) in predicting both bypass and orderly transitions in channel flow at target Reynolds numbers of $\mathrm{Re}_\tau = 130$ and 200, respectively. Predictions of bypass transition initiated from localized initial disturbances agree well with direct numerical simulation. For orderly transition, we simulate K- and H-type transitions, due to the interaction of two- and three-dimensional instability waves. We show good predictions for both scenarios, with a slight delay in the transition time. The WMSOM approach offers a significant reduction in computational cost compared to wall-resolved LES.

DOI: 10.1103/PhysRevFluids.6.074608

I. INTRODUCTION

The transition to turbulence in wall-bounded flows leads to a significant increase in viscous losses and wall heat transfer, which has important practical implications, e.g., in turbomachinery [1]. Owing to this practical importance, modeling the transition process is an important challenge. In boundary layers and channel flows, the laminar-turbulent transition is often classified as either orderly (natural) [2] or a bypass transition [3,4]. The orderly scenario is mediated by Tollmien-Schlichting instability waves which form, amplify, undergo secondary instability, and ultimately lead to the formation of λ-shaped vortices that become sites for the breakdown to turbulence. Based on the arrangement of the λ vortices, the orderly transition can be further classified as fundamental (K-type) or subharmonic (e.g., H-type) [5,6]. The other route to turbulence, termed bypass transition [7], encompasses all scenarios that do not fit the orderly description. The most common case of bypass transition takes place when wall-bounded flows are exposed to vortical forcing, which leads to the amplification of streamwise-elongated streaks through lift-up mechanism [8,9], followed by secondary instability [10,11] and nonlinear breakdown into turbulence spots [12].

The traditional computational approaches to study these transition mechanisms has been by performing either stability analyses [6,13] or direct numerical simulation (DNS) [14–16]. Stability analyses involve using the linearized Navier-Stokes (NS) equations from which the different

instability mechanisms that lead to the growth of perturbation amplitude can be investigated. However, owing to the linear nature of the governing equations, the nonlinear interactions responsible for the transition to turbulence are not captured. Conversely, DNS of the laminar-turbulent transition process avoids this drawback since the full NS equations are used and it is possible to simulate the complete transition process. Nevertheless, due to the wide range of spatial and temporal scales involved, performing DNS is computationally expensive in general, including DNS of the laminar-turbulent transition. As an alternative, large eddy simulation (LES) that has lesser computational cost than DNS [17,18] can be considered for studying the laminar-turbulent transition [19–21]. Large eddy simulation can be performed by either resolving [wall-resolved LES (WRLES)] or modeling [wall-modeled LES (WMLES)] the inner layer of a turbulent flow [22,23]. Wall-modeled LES can be computationally much less expensive than WRLES.

Various studies [19,24,25] have shown the transition to turbulence in wall-bounded flows using WRLES. In [19], the natural transition in a plane channel flow is simulated using a scaled Smagorinsky model. The eddy viscosity in the scaled Smagorinsky model is modified using a scaling factor based on the shape factor for laminar and equilibrium turbulent flow. The scaling factor decreases subgrid scale (SGS) dissipation in the laminar stages of transition. In [24], the ability of WRLES in predicting K- and H-type transition mechanisms in a boundary layer was tested using different SGS models. It was observed that the LES with a constant Smagorinsky model did not undergo transition as the laminar fluctuations were damped by the SGS stress, whereas dynamic SGS models had negligible eddy viscosity in the laminar regions, enabling transition to occur at the right location. However, the dynamic SGS models on a coarser grid underpredicted the skin friction overshoot in the fully turbulent regions. In [25], LES of bypass transition in a boundary layer was studied whose properties were matched with experiments by applying a constant Smagorinsky model. An empirical low-Reynolds-number laminar correction suggested in [26] was applied to damp the eddy viscosity in the laminar regions of the flow similar to the idea used in [19].

In WMLES, the most frequently used approach is the equilibrium wall model which assumes the near-wall flow is in near equilibrium with the velocity profile exhibiting a universal logarithmic profile. This assumption enables relating the velocity at some distance to the wall to the wall stress [22,23,27]. However, applying WMLES in a transitional flow would predict wrong wall stresses in the laminar regions, hence possibly not capturing the correct transition mechanism or location. In order to alleviate this problem, in [28] a sensor-based WMLES approach was used to simulate a laminar-turbulent transition. The sensor identifies laminar and turbulent regions of the flow. Once the distinction is made, the wall model is selectively applied only in the turbulent regions while a standard no-slip boundary condition is applied in the laminar regions. Reference [28] used a sensor based on the turbulent kinetic energy to distinguish the turbulent and nonturbulent regions of the transitional flow. The WMLES with this sensor rightly predicted the wall stresses in the transitional regions of the boundary layer. The transition location from WMLES also matched with the DNS. However, a threshold for the sensor needed to be prescribed to classify a point in the flow as either laminar or turbulent. Having to specify thresholds requires *ad hoc* user input, which is often undesirable if one wishes to avoid having to tune a model.

In the present study, a different sensor-based WMLES of the transition processes is investigated. Instead of using turbulent kinetic energy with a subjectively chosen threshold as the sensor, turbulent/nonturbulent (T/NT) classification is performed using a self-organizing map (SOM). This classifier uses a type of k-means clustering technique, one of several unsupervised-learning algorithms discussed in [29]. Alternative methods exist [29] such as the unsupervised spectral clustering algorithm and supervised-learning classifiers. For supervised-learning methods, the training data must be labeled beforehand as turbulent or nonturbulent, and a threshold needs to be selected for training the classifier. Since the SOM unsupervised-learning method does not require such labeling and threshold choices even during training, we find it preferable for the present applications while stressing that the SOM is by no means the only possible tool that can be applied for machine-learning-based T/NT classification. The details of the T/NT classification method used in this paper are explained in Sec. II. The governing equations for the LES are discussed in Sec. III.

Transitions by both orderly and bypass mechanisms are investigated in this study. The key results for the bypass transition are discussed in Sec. IV and for the orderly transition in Sec. V. The study's main conclusions are summarized in Sec. VI.

II. SOM TRAINING AND T/NT CLASSIFICATION

In this section, the T/NT classification using the SOM and its application in WMLES are discussed. In a recent study [30], the SOM was introduced for T/NT classification. The method was subsequently applied to study the fractal dimension of the T/NT interface that surrounds turbulent spots [31] using DNS data of a transitional boundary layer [32]. In the approach, every spatial location in the flow is characterized as either turbulent or nonturbulent using a 16-dimensional data vector $\boldsymbol{X}$ which contains the magnitudes of total velocity (if the problem is formulated in a frame in which the wall moves, then the input should be the velocity relative to the wall), fluctuating velocity, velocity gradient components, and streamwise and wall-normal coordinates,

$$\boldsymbol{X} = \left[|u|, |v|, |w|, |u'|, |v'|, \left|\frac{\partial u}{\partial x}\right|, \left|\frac{\partial u}{\partial y}\right|, \left|\frac{\partial u}{\partial z}\right|, \left|\frac{\partial v}{\partial x}\right|, \left|\frac{\partial v}{\partial y}\right|, \left|\frac{\partial v}{\partial z}\right|, \left|\frac{\partial w}{\partial x}\right|, \left|\frac{\partial w}{\partial y}\right|, \left|\frac{\partial w}{\partial z}\right|, x, y \right]. \quad (1)$$

Since the streamwise direction is nonperiodic in the transitional boundary layer, x was included in the input vector for training [30]. Each input is normalized by its global standard deviation computed over the entire domain containing both turbulent and laminar regions in the transitional boundary layer data set. Given this input vector for the training data, the SOM seeks to identify two distinct clusters. On output, it gives the coordinates of the two nodes, or the centroids, of T/NT clusters in the 16-dimensional hyperspace. From these coordinates, the equation of the hyperplane that bisects the T/NT clusters in the hyperspace,

$$\boldsymbol{a} \cdot \boldsymbol{X} + 1 = 0, \quad (2)$$

is obtained. In Eq. (2), $\boldsymbol{a}$ is the weight vector or the coefficients associated with each input. At a given point, if $\boldsymbol{a} \cdot \boldsymbol{X} + 1 < 0$, the point is characterized as turbulent and if $\boldsymbol{a} \cdot \boldsymbol{X} + 1 > 0$ it is nonturbulent. Hence, the SOM allows us to classify the T/NT regions without using any subjectively chosen threshold value (the value of 1 is the SOM method context-independent default value). An additional postprocessing step is required since the resulting turbulent regions of the flow still contain many very small regions of "holes" that should be considered part of the turbulent region. In [30], these laminar hole regions were reclassified into turbulent regions through a standard hole filling postprocessing step. In Ref. [30] it was shown that the set of variables in Eq. (1) provided very good results (i.e., there was no motivation to increase the number of variables). Conversely, none of the coefficients of the vector $\boldsymbol{a}$ were found to be significantly smaller than others, so decreasing the number of variables also was not called for. In the present work we therefore elect to use the tested methodology documented in detail in [30] without further modifications (except omission of the streamwise coordinate x when applying the method to channel flow that is homogeneous in the streamwise direction).

In the present study, LES of laminar-turbulent transition in a pressure-driven channel flow is targeted, while in [30] the SOM was applied to a spatially developing transitional boundary layer. There, any given snapshot contained both laminar and turbulent regions at any given time and a single snapshot could thus be used for training. To obtain the corresponding SOM coefficients (training) for a channel flow, snapshots at different times must be considered in order to include data from both laminar and turbulent regions. For SOM training for channel flow, we use a DNS in which the flow starts in a laminar Poiseuille state and localized perturbations are added to it (more details are provided in Sec. IV). The flow undergoes a transition and at some later time becomes fully turbulent and statistically in equilibrium. A laminar snapshot ($t = 0$) and a fully turbulent snapshot ($t = 282$) are chosen from such a DNS and combined together as the training data. The training data set is chosen such that it contains about the same number of points in a laminar and

TABLE I. Computational domain size and grid points for DNS of localized perturbation.

Re	Domain size $L_x \times L_y \times L_z$	No. of grid points $N_x \times N_y \times N_z$	Re_τ	Grid resolution $\Delta x^+ \times \Delta y^+_{\mathrm{min}} \times \Delta z^+$
2000	$48 \times 2 \times 24$	$384 \times 384 \times 384$	134.71	$17 \times 0.7 \times 8$

turbulent state. The code used for the DNS is described in the next section, and the computational domain size and grid resolution used for DNS of transitional channel flow are given in Table I.

The input vector $\boldsymbol{X}$ in Eq. (1) is constructed from the training data. Because the streamwise coordinate x is in a periodic direction for the channel, it is not included in $\boldsymbol{X}$, which becomes a 15-dimensional vector. The input vector is then normalized by the standard deviation of each of its elements and SOM training is performed to obtain the coefficients $\boldsymbol{a}$ of the hyperplane equation (2). Table II lists the input vector $\boldsymbol{X}$ of normalized variables, global standard deviation σ used for normalizing the original vector element data, and the SOM coefficient vector $\boldsymbol{a}$ that results from the training.

Additional tests including training data during transition did not yield significantly different hyperplane parameters and hence we opted to train using only a laminar and fully turbulent data set. The same standard deviation σ and the SOM coefficients $\boldsymbol{a}$ obtained from the training of DNS snapshots are used in the WMLES of transitional channel flow. Also here the laminar hole regions in the resulting T/NT contours are filled using morphological operations with a single cycle of binary dilation followed by erosion [33] (see Fig. 1).

Once the laminar and turbulent regions of the flow are classified in the LES, the wall stress boundary condition from the wall model is applied only in the turbulent regions of the flow, while a standard no-slip boundary condition is applied in the laminar regions,

$$\boldsymbol{\tau}_w = \begin{cases} \boldsymbol{\tau}_{w,\mathrm{wm}} & \text{if } \boldsymbol{a} \cdot \boldsymbol{X} + 1 < 0 \text{ (turbulent)} \\ \boldsymbol{\tau}_{w,\mathrm{ns}} & \text{if } \boldsymbol{a} \cdot \boldsymbol{X} + 1 > 0 \text{ (nonturbulent)}, \end{cases} \tag{3}$$

where $\boldsymbol{\tau}_{w,\mathrm{wm}}$ is the wall stress obtained using an equilibrium wall model (described in more detail in Appendix A) and $\boldsymbol{\tau}_{w,\mathrm{ns}}$ is the wall stress assuming no-slip boundary condition. Similarly, in the subgrid model used for LES (more details provided in Sec. III and Appendix B), the total viscosity is chosen according to

$$\nu_{\mathrm{tot}} = \begin{cases} \nu + \nu_T & \text{if } \boldsymbol{a} \cdot \boldsymbol{X} + 1 < 0 \text{ (turbulent)} \\ \nu & \text{if } \boldsymbol{a} \cdot \boldsymbol{X} + 1 > 0 \text{ (nonturbulent)}, \end{cases} \tag{4}$$

where ν and ν_T are the molecular and turbulent subgrid-scale viscosities, respectively. The capability of such a wall-modeled LES with T/NT classification in predicting the transition processes is investigated in the following sections.

TABLE II. Input vector $\boldsymbol{X}$ normalized by standard deviation σ and the corresponding SOM coefficients $\boldsymbol{a}$.

Input No.	Description	Expression $\boldsymbol{X}$	Standard deviation σ	SOM coefficient $\boldsymbol{a}$
1–3	velocity	$\lvert u\rvert, \lvert v\rvert, \lvert w\rvert$	0.371, 0.023, 0.031	−0.0147, −0.1226, −0.1168
4–5	perturbation velocity	$\lvert u'\rvert, \lvert v'\rvert$	0.06, 0.023	−0.1154, −0.1226
6–14	velocity gradient	$\lvert\partial u/\partial x\rvert, \lvert\partial u/\partial y\rvert, \lvert\partial u/\partial z\rvert$	0.108, 1.77, 0.323	−0.1154, 0.0341, −0.109
		$\lvert\partial v/\partial x\rvert, \lvert\partial v/\partial y\rvert, \lvert\partial v/\partial z\rvert$	0.061, 0.151, 0.124	−0.1155, −0.1154, −0.1178
		$\lvert\partial w/\partial x\rvert, \lvert\partial w/\partial y\rvert, \lvert\partial w/\partial z\rvert$	0.078, 0.358, 0.133	−0.1196, −0.0918, −0.1187
15	wall normal height	y	0.58	-2.314×10^{-4}

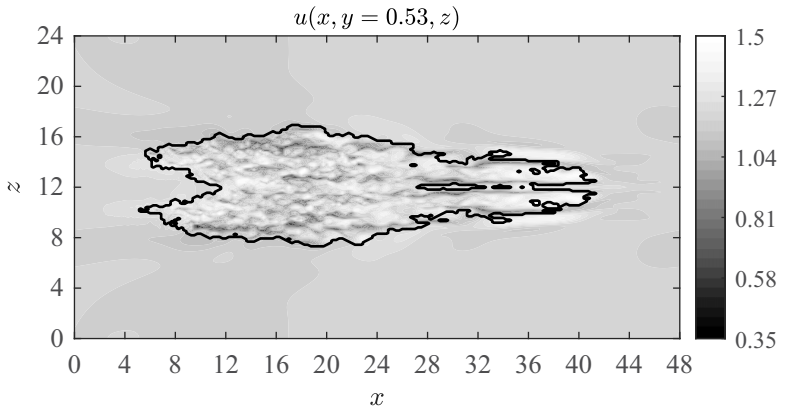

FIG. 1. Streamwise velocity u contour from DNS training data with the T/NT interface at $y = 0.53$.

III. LARGE EDDY SIMULATION EQUATIONS, MODELS, AND NUMERICAL METHODS

The governing Navier-Stokes equations for the filtered velocity and pressure are

$$\frac{\partial \tilde{u}_i}{\partial x_i} = 0, \tag{5}$$

$$\frac{\partial \tilde{u}_i}{\partial t} + \frac{\partial \tilde{u}_i \tilde{u}_j}{\partial x_j} = -\frac{\partial \tilde{p}}{\partial x_i} + \frac{\partial \tilde{\tau}_{ij}}{\partial x_j} - \frac{\partial \tau_{ij}^{\mathrm{SGS,d}}}{\partial x_j}. \tag{6}$$

The tilde represents spatial filtering, $\tilde{u}_i = (\tilde{u}, \tilde{v}, \tilde{w})$, $x_i = (x, y, z)$, $\tilde{\tau}_{ij} = 2\nu \tilde{S}_{ij}$ is the viscous stress tensor, and $\tau_{ij}^{\mathrm{SGS,d}} = -2\nu_T \tilde{S}_{ij}$ is the deviatoric part of the subgrid-scale stress tensor modeled using the eddy viscosity model. The SGS eddy viscosity ν_T is evaluated as

$$\nu_T = C_s^2 \tilde{\Delta}^2 |\tilde{S}|. \tag{7}$$

Here $|\tilde{S}| = (2\tilde{S}_{lm}\tilde{S}_{lm})^{1/2}$ and $\tilde{\Delta} = (\Delta x \Delta y \Delta z)^{1/3}$ are the filter length scale and the model coefficient C_s^2 is obtained from the dynamic Smagorinsky SGS model [34,35] with a nondynamic correction for scale dependence that is necessary in WMLES [36]. Details of the SGS model are discussed in Appendix B. When run in DNS mode, the code is used with $\tau_{ij}^{\mathrm{SGS,d}} = 0$. The wall boundary condition can be either no slip at the walls for DNS or WRLES or a prescribed wall stress for imposition of an explicitly fitted equilibrium wall model. More details about the wall model are provided in Appendix A.

The TRANSFLOW solver [37,38] adopted in this work uses a control volume formulation in generalized curvilinear coordinates [39] to discretize the filtered Navier-Stokes equations (6). The fractional-step method is adopted, with an explicit Adams-Bashforth scheme used for temporal discretization of the nonlinear advection terms; the diffusion terms are advanced using implicit Crank-Nicolson scheme. The pressure Poisson equation is solved to enforce mass conservation using a Fourier transform in the streamwise and spanwise directions with tridiagonal inversion in the wall-normal direction.

The wall boundary condition is imposed using a ghost cell approach. TRANSFLOW uses a staggered grid with velocity fluxes stored at cell faces and pressure at cell centers. The wall stresses $\tilde{\tau}_{yx,w}$ and $\tilde{\tau}_{yz,w}$ corresponding to either no-slip condition or the wall model are evaluated or modeled, respectively, for each computational cell at the wall. Wall stresses along with no-penetration ($\tilde{v} = 0$) condition are then applied as the boundary condition using the velocities at the first grid point ($\tilde{\boldsymbol{u}}_1$)

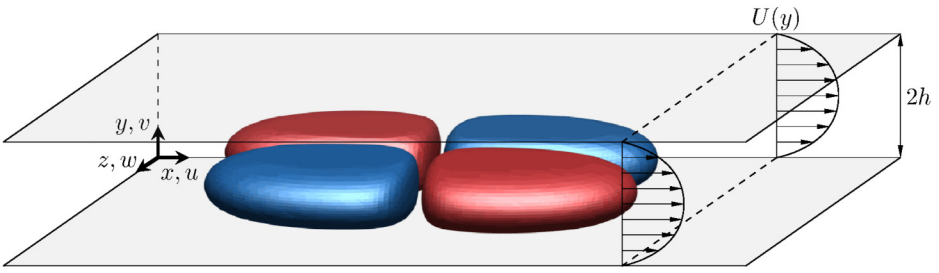

FIG. 2. Schematic of the computational domain with the base flow, and the initial perturbation visualized using isosurfaces of streamwise vorticity $\tilde{\omega}_x$. The isosurfaces shown correspond to $\tilde{\omega}_x = +0.003$ (red) and $\tilde{\omega}_x = -0.003$ (blue).

from the wall and at the ghost cell ($\tilde{\boldsymbol{u}}_g$) that are a distance Δy apart,

$$\tilde{\tau}_{yx,w} = \nu\left(\frac{\tilde{u}_1 - \tilde{u}_g}{\Delta y}\right), \quad \tilde{\tau}_{yz,w} = \nu\left(\frac{\tilde{w}_1 - \tilde{w}_g}{\Delta y}\right). \tag{8}$$

In (8), for given wall-modeled stresses $\tilde{\tau}_{xy,w}$ and $\tilde{\tau}_{yz,w}$, the corresponding ghost cell velocities $\tilde{\boldsymbol{u}}_g$ are obtained, which in turn impose the required wall stress boundary condition. For imposition of the no-slip boundary condition in the laminar regions, $\tilde{\boldsymbol{u}}_g$ is prescribed as usual so as to be consistent with the no-slip condition at the wall.

In this study, the code is applied to perform LES of the laminar-turbulent transition in channel flow through bypass as well as orderly transition routes. The transition through a bypass route discussed in Sec. IV is achieved by introducing a localized three-dimensional (3D) perturbation in the Poiseuille base flow. The orderly transition discussed in Sec. V also starts with a Poiseuille base flow but perturbed by 2D Tollmien-Schlichting and 3D oblique waves. In both cases, results from wall-modeled LES with T/NT classification (WMSOM) are compared against results from DNS, WRLES, and WMLES without T/NT classification.

IV. RESULTS: BYPASS TRANSITION

Simulations of laminar-turbulent transition through the bypass mechanism uses the computational domain shown in Fig. 2. The Reynolds number of the flow based on the bulk velocity U_b and half-channel height h is $\mathrm{Re} = U_b h/\nu = 2000$. The domain size and the grid parameters for the DNS, WRLES, and WMLES/WMSOM are given in Table III. We investigate the evolution of a 3D localized perturbation in the presence of the base flow very similar to prior cases that were studied using DNS [16,37].

TABLE III. Computational domain size and grid points for LES and DNS of the bypass transition. Here y_{wm} is the wall-model height.

Case	Re	Domain size $L_x \times L_y \times L_z$	No. of grid points $N_x \times N_y \times N_z$	Re_τ	Grid resolution $\Delta x^+ \times \Delta y^+_{\mathrm{min}} \times \Delta z^+$	y_{wm}
DNS [37]	2000	$48 \times 2 \times 24$	$1024 \times 400 \times 512$	132.05	$6.19 \times 0.03 \times 6.19$	
WRLES	2000	$48 \times 2 \times 24$	$204 \times 128 \times 100$	114	$27 \times 0.2 \times 27$	
WMLES/WMSOM	2000	$48 \times 2 \times 24$	$100 \times 20 \times 50$	130	$62 \times 13 \times 62$	0.25

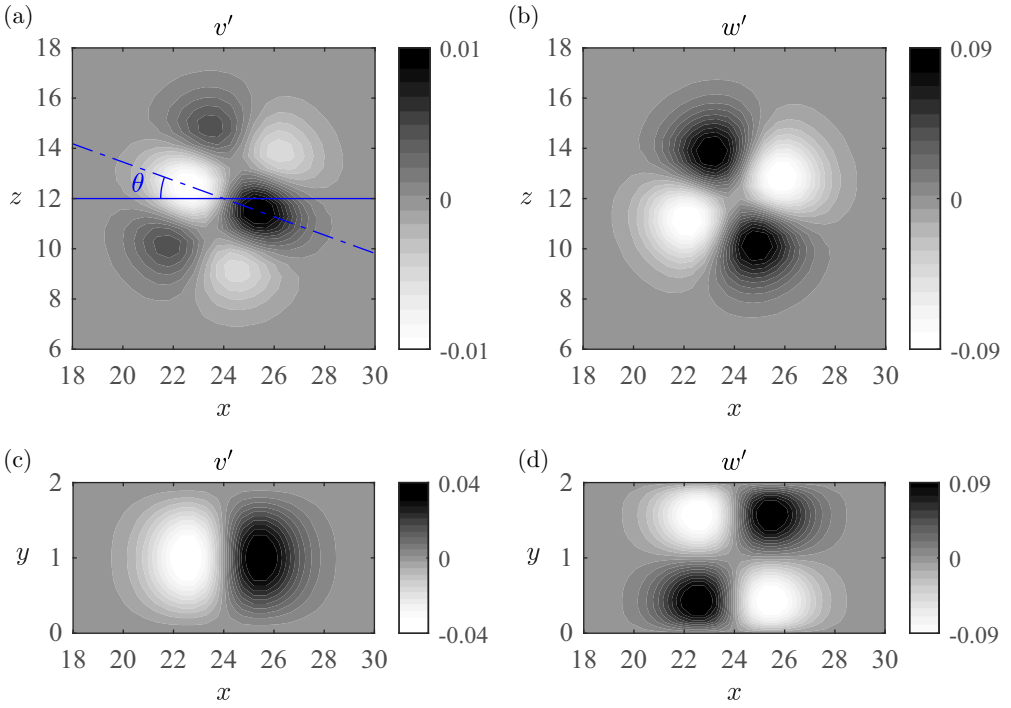

FIG. 3. Large-amplitude ($\epsilon = 0.2097$) localized perturbation contours of (a) v' and (b) w' with $\theta = 20^\circ$ at $y = 0.25$. The contours of (c) v' and (d) w' at $z = 12.96$ are from the initial perturbation with $\theta = 0^\circ$.

A. Initial condition

The initial velocity field for the bypass transition consists of Poiseuille base flow and a localized perturbation

$$\boldsymbol{u}(\boldsymbol{x}, t = 0) = \tfrac{3}{2}[1 - (y-1)^2]\boldsymbol{e}_x + \boldsymbol{u}'(\boldsymbol{x}, t = 0), \tag{9}$$

where

$$\begin{aligned}
\boldsymbol{u}'(\boldsymbol{x}, t = 0) = (u', v', w') &= \left(-\frac{\partial \psi}{\partial y}\sin\theta, \frac{\partial \psi}{\partial z'}, -\frac{\partial \psi}{\partial y}\cos\theta\right), \\
\psi &= \epsilon f(y)\left(\frac{x'}{l_x}\right) z' \exp\left[-\left(\frac{x'}{l_x}\right)^2 - \left(\frac{z'}{l_z}\right)^2\right], \\
x' &= x\cos\theta - z\sin\theta, \quad z' = x\sin\theta + z\cos\theta, \\
f(y) &= y^p(2-y)^q.
\end{aligned} \tag{10}$$

The perturbation (10) takes the form of two pairs of counterrotating vortices as shown in Fig. 2. This was first proposed in [40] and was later generated experimentally in [41]. The ψ is the stream function of the perturbation with initial orientation θ. The function $f(y)$ ensures that the disturbance is zero at the boundaries. The decay length scales of the perturbation are $l_x = 2$ and $l_z = 2$, and $p = 2$ and $q = 2$ are used for the function $f(y)$. In this study, the time evolutions of perturbations with different initial orientations $\theta = 0^\circ, 10^\circ, 20^\circ, 45^\circ$ and two different amplitudes $\epsilon = 1.5 \times 10^{-4}$ (small) and 0.2097 (large) are considered. The contours of v' and w' with $\theta = 0^\circ$ and 20° of the large-amplitude perturbation are shown in Fig. 3.

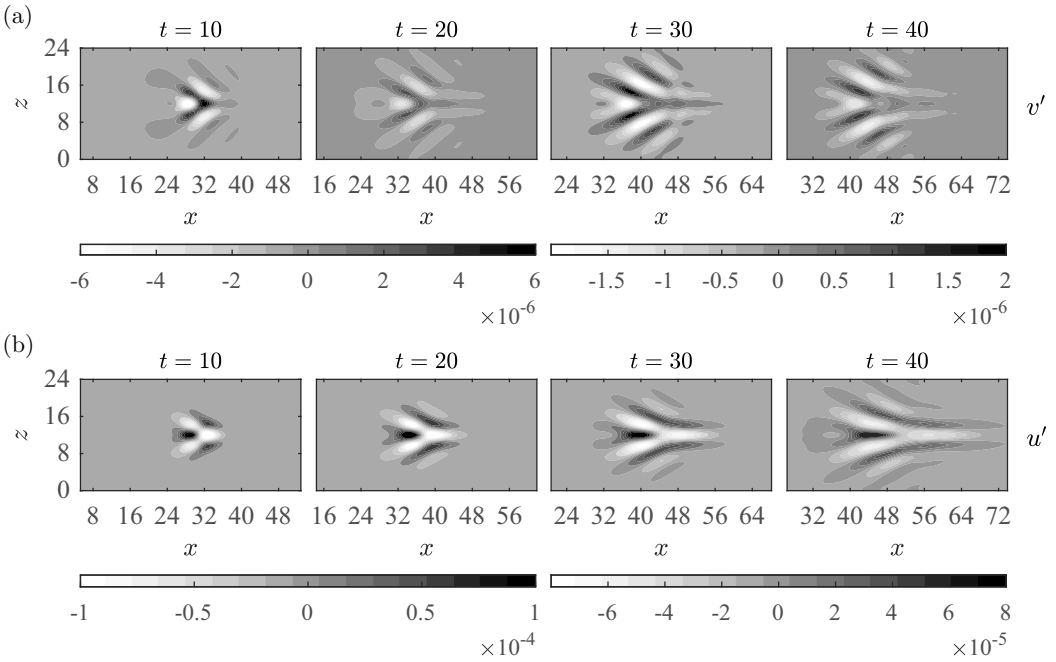

FIG. 4. Evolution of small-amplitude ($\epsilon = 1.5 \times 10^{-4}$ and $\theta = 0^\circ$) (a) v' and (b) u' perturbation at $y = 0.25$ and $t = 10, 20, 30, 40$.

Prior DNS of the time evolution of such localized perturbations [16,37] showed that the laminar-turbulent transition starts with an initial linear stage characterized by amplification of streamwise perturbation through a lift-up mechanism. The disturbance is further amplified owing to secondary instability leading to the formation of a turbulent spot which marks the final stage of the breakdown to turbulence. Here the bypass transition of the localized perturbation is simulated using the WMSOM method described in Sec. II. The computational cost of this LES is much smaller than the DNS since the WMSOM is performed with a grid resolution that is roughly ten times coarser in each direction than the DNS (Table III). In the following sections, simulations of the evolution of small- and large-amplitude localized perturbations using the WMSOM are discussed.

B. Wall-modeled LES of evolution of small-amplitude perturbations

In this section the evolution of a small-amplitude ($\epsilon = 1.5 \times 10^{-4}$) disturbance with initial orientations $\theta = 0^\circ, 10^\circ, 20^\circ, 45^\circ$ is presented and discussed. The perturbation velocities $\boldsymbol{u}' = (u', v', w')$ at different instances of the evolution are obtained from the total velocity field $\boldsymbol{u}$ using

$$\boldsymbol{u}'(x, y, z, t) = \boldsymbol{u}(x, y, z, t) - \langle \boldsymbol{u} \rangle_{xz}(y, t), \tag{11}$$

where $\langle \boldsymbol{u} \rangle_{xz}$ is the instantaneous mean flow obtained by horizontal planar averaging. From prior DNS studies [16], it is known that the small-amplitude perturbation does not lead to a transition to a turbulent state for any of the orientations; the flow remains laminar throughout the evolution. There is only an initial transient growth of the energy which is associated with the non-normality of eigenfunctions from the linear stability equations [42]. For longer times, the viscous dissipation dominates and the energy decays in time.

In Figs. 4(a) and 4(b), the transient growth and viscous decay of the localized perturbation with $\theta = 0^\circ$ are shown. In Fig. 4(a), the v' structure is dispersive and its magnitude is smaller than u', although the strength of the streamwise perturbation is zero initially. The u' also becomes

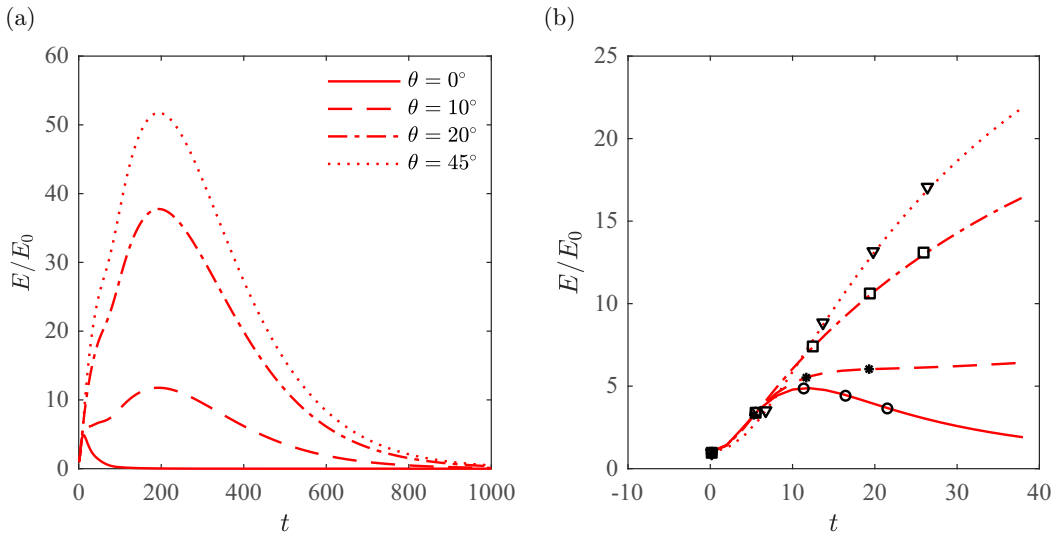

FIG. 5. Total perturbation kinetic energy for small-amplitude localized disturbance ($\epsilon = 1.5 \times 10^{-4}$): (a) energy decay for different initial orientations and (b) comparison between the WMSOM (red lines) and DNS (black markers) [16]. Here $E_0 = E(t = 0)$ is initial energy of the perturbation.

elongated downstream. This transient growth of u' is associated with the lift-up mechanism where the u' grows linearly in time owing to forcing of wall-normal vorticity by wall-normal velocity. The transient growth is larger for small streamwise wave numbers, leading to an elongated shape for the u' perturbation.

The total perturbation kinetic energy

$$E(t) = \frac{1}{L_x L_y L_z} \int_0^{L_x} \int_0^{L_y} \int_0^{L_z} \frac{1}{2}(u'^2 + v'^2 + w'^2) dx\, dy\, dz \tag{12}$$

is computed at each time step and its evolution is plotted in Fig. 5(a). An enlarged view near the initial linear growth region ($0 < t < 40$) is shown in Fig. 5(b). The energy evolution from the WMSOM (red lines) agrees well with the energy evolution from DNS (black markers) from [16]. The fact that the SOM in the WMSOM correctly characterizes all of the points in the domain as laminar for the small-amplitude perturbation ensures that wall and SGS models are not activated anywhere in this flow. Even with different initial orientations, where the disturbance with $\theta = 45°$ undergoes the largest amplification, the SOM still treats the flow as laminar. Note that the initial perturbation is of relatively large size and is therefore well resolved initially even at the LES resolution. Hence, the results from the WMSOM of small-amplitude perturbations validate the proper, albeit trivial, working of the SOM in this case. Also, the excellent agreement with DNS observed in Fig. 5(b) provides supporting evidence for the accuracy of the numerical code used in this study.

C. Wall-modeled LES of bypass transition with large-amplitude perturbation

In this section the time evolution of large-amplitude perturbation ($\epsilon = 0.2097$) is discussed, with initial orientation $\theta = 0°$. The wall stress (τ_w) contours from the WRLES, WMLES, and WMSOM at the wall-model height $y = 0.25$ and times $t = 20, 80, 110, 300$ are shown in Figs. 6(a)–6(c). The time evolutions of Re_τ from LES and DNS are plotted together for comparison in Fig. 6(d). The vertical dotted lines are the times at which the contours are plotted. At $t = 20$, the region of the localized disturbance from all the LES cases has a higher wall stress than the surrounding regions.

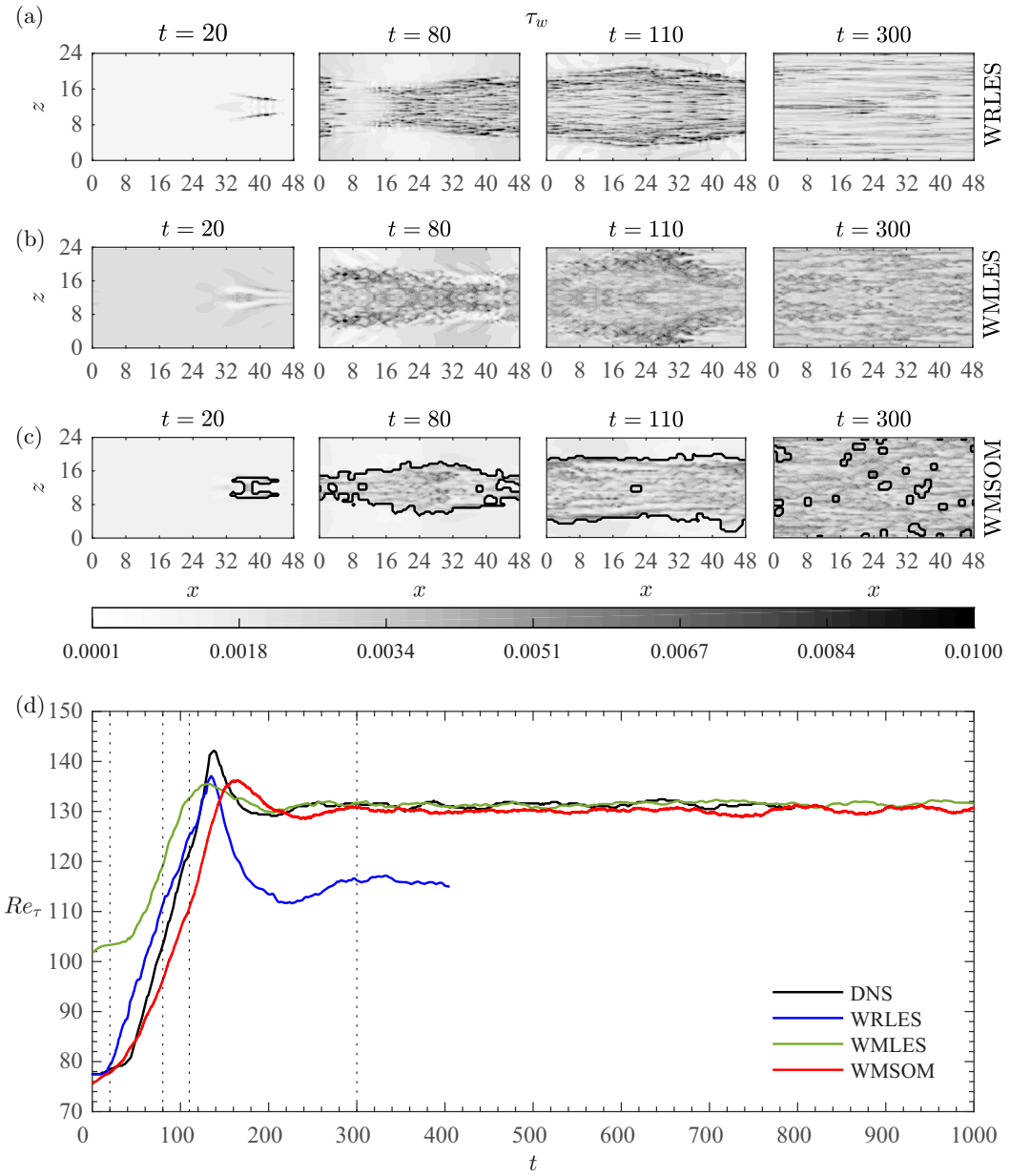

FIG. 6. Contours of wall stress τ_w at $y = 0$ and $t = 20, 80, 110, 300$ from the (a) WRLES, (b) WMLES, and (c) WMSOM (black solid lines represent the T/NT interface). (d) Time evolution of Re_τ from LES and DNS [37]. Vertical dotted lines correspond to the time at which the contours are plotted.

The SOM [Fig. 6(c)] identifies the perturbation as turbulent and the points surrounding it as laminar. In the Re_τ plot, $t = 20$ occurs before the overall transition. Therefore, the flow is laminar and the SOM rightly identifies the T/NT interface as enclosing only a very small portion of the overall domain.

The wall stress from WMLES (without the SOM) is noticeably higher than the WRLES and WMSOM cases. The equilibrium wall model assumes the flow is stationary and the wall stress is

obtained from a turbulent mean flow profile, even in a wall model that smoothly merges between the viscous sublayer and the logarithmic layer as used here (see Appendix A). When this wall model is applied to a laminar flow, the corresponding wall stress can be significantly higher than the wall stress inferred from a no-slip boundary condition. This is evident in Fig. 6(d), where the Re_τ for WMLES in the laminar and transitional regions are higher than the Re_τ from the WRLES and WMSOM.

In the DNS [37] of the large-amplitude perturbation, a secondary instability leads to the formation of a turbulent spot that spreads and fills the domain, thus leading to a fully turbulent state. The formation of the turbulent spot occurs at around $t = 40$. This is also the time at which the Re_τ increases from its laminar value and reaches a turbulent state for $t > 200$. The transition time of WRLES is slightly before the DNS, while the WMSOM is closer to the DNS. Once the turbulent spot is formed, it advects downstream and spreads the turbulence in the entire domain. This is seen in the wall stress contours of Figs. 6(a)–6(c) at $t = 80, 110$ for all the LES cases. In the contour from WMSOM, the SOM clearly separates the growing spot from the laminar flow surrounding it. The growth of the spot is similar for the WMSOM and WRLES. A higher wall stress from the wall model leads to a larger growth of the perturbation in the WMLES case. Note that, like other sharp sensor-based methods, the WMSOM approach introduces sharp switches between the modeled wall and SGS stresses at the interface. In our present applications, no adverse numerical effects are observed from this model feature. However, if numerical problems were to arise, e.g., in the context of other numerical methods, a smoothing operation based, e.g., on the distance to the SOM hyperplane could be envisioned. The Re_τ from WMSOM is underpredicted compared to the DNS in the transitional regime. This mismatch can arise due to a slower spreading rate of the spot, a lower prediction of the stress within the spot, or a combination of both factors. The latter is more likely since the ensemble-averaged stress within the spot is spatially heterogeneous [43], while the WMSOM assumes equilibrium within the identified turbulent region.

At $t = 300$, the flow has reached a fully turbulent state for all the cases and Re_τ has reached an equilibrium value. In the WMSOM contour, the SOM identifies most of the regions as turbulent with small islands of nonturbulent regions. Even in the presence of these nonturbulent regions, the Re_τ closely agrees with the DNS. Noticeably, for the WRLES, the Re_τ in the stationary state is underpredicted. A similar underprediction of the friction coefficient was reported in [24] in the case of boundary layer transition. In that study, the friction coefficient underprediction was attributed to inadequate reproduction of SGS stresses, which could also be at play here. It was also shown that refining the grid leads to a better match of the friction coefficient between WRLES and DNS.

In order to ensure that the WMSOM is robust, we vary the orientation angle of the initial disturbance. The time evolution of $|u'|$ and Re_τ from WMSOM is shown in Figs. 7(a) and 7(b). All cases undergo transition to a stationary state, as is evident from the saturated Re_τ [Fig. 7(b)]. Increasing the orientation angle of the initial perturbation delays the transition slightly. Whether the earlier disturbance amplification plays a role will be examined; here we only note that in linear theory streamwise rolls lead to the most amplifying response in wall-bounded shear flows [42]. However, with interest in the transition, the late stages including secondary instability and energy cascade all contribute to the onset and increase in intermittency as we approach a fully turbulent state.

At $t = 20$ [Fig. 7(a)], the turbulent spot structures of the different initial conditions vary significantly from each other. For $\theta = 0^\circ$, the spot structure is symmetric and the entire core region of the perturbation is classified as turbulent by the SOM. For $\theta = 10^\circ$, the spot is asymmetric with the larger region in $z > 12$ classified as turbulent. When the orientation angle is increased to $\theta = 20^\circ$, the spot structure is again asymmetric. The perturbation in $z < 12$ is much weaker than the disturbance with the $\theta = 0^\circ$ and 10° cases. A similar scenario is seen for the $\theta = 45^\circ$ case. However, the turbulent region is smaller than the other cases, leading to a lower value of Re_τ for $\theta = 45^\circ$ as seen in Fig. 7(b).

At a later time $t = 80$, the spot has grown in size and turbulence is spread throughout the streamwise extent of the channel. The turbulent spot size of the $\theta = 45^\circ$ case is slightly smaller

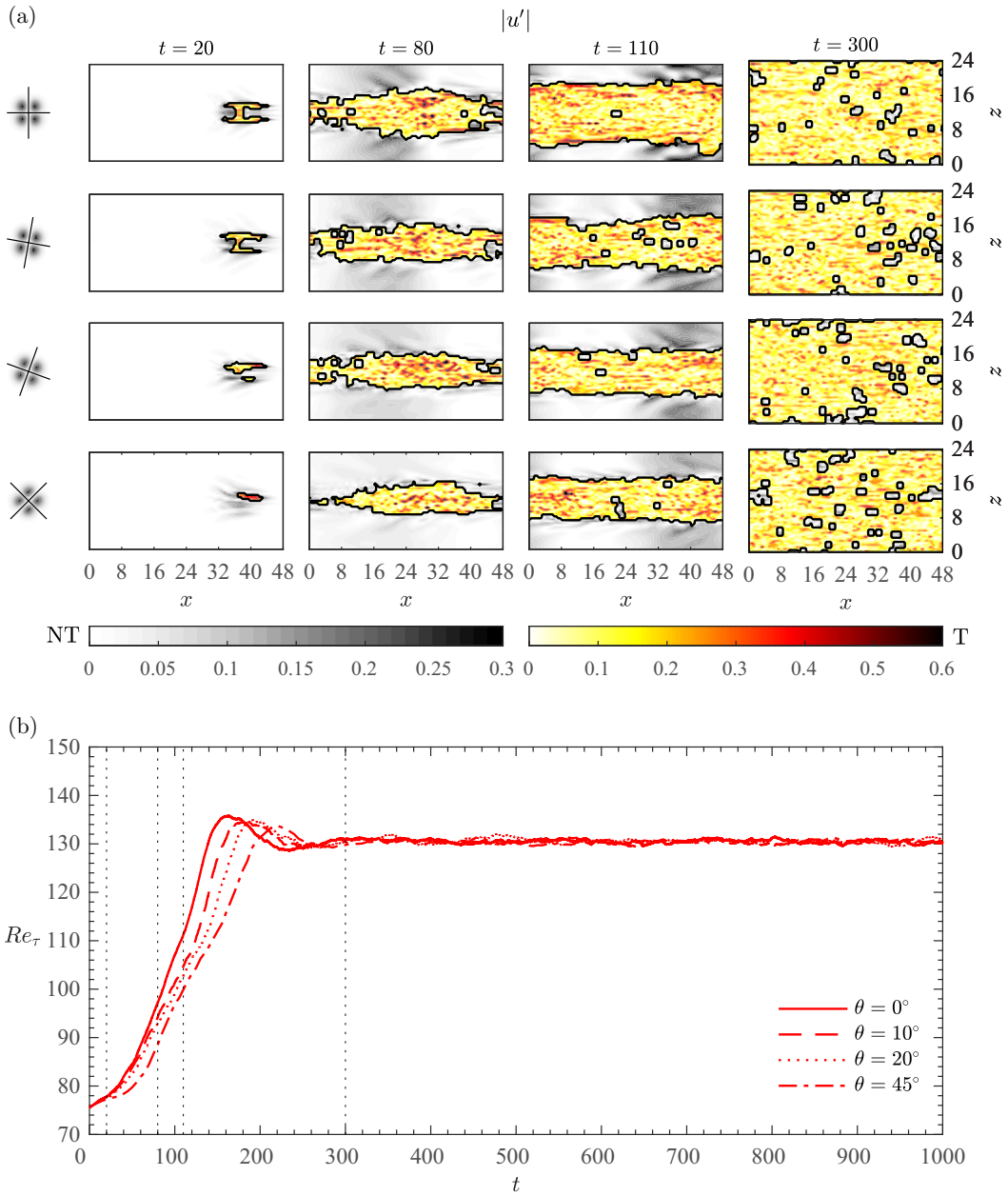

FIG. 7. (a) Contours of $|u'|$ with the T/NT interface (black line) at $y = 0.25$ and $t = 20, 80, 110, 300$ and (b) time evolution of Re_τ from the WMSOM for different initial orientations $\theta = 0°, 10°, 20°, 45°$. Vertical dotted lines correspond to the time at which the contours are plotted. The contours of $|v'| + |w'|$ at $t = 0$ with axes are plotted on the left side of $t = 20$ contours. Grayscale and hot colormaps represent nonturbulent (NT) and turbulent (T) regions, respectively.

than the other cases as the transition progresses more slowly for this case. Regardless of the angle, however, once the spots are formed a transition to a fully turbulent state seems inevitable in this configuration. The final state is also statistically similar among all cases, with the Re_τ saturating around 130, which is very close to the DNS [37] value of $\mathrm{Re}_\tau = 132$ for $\theta = 0°$.

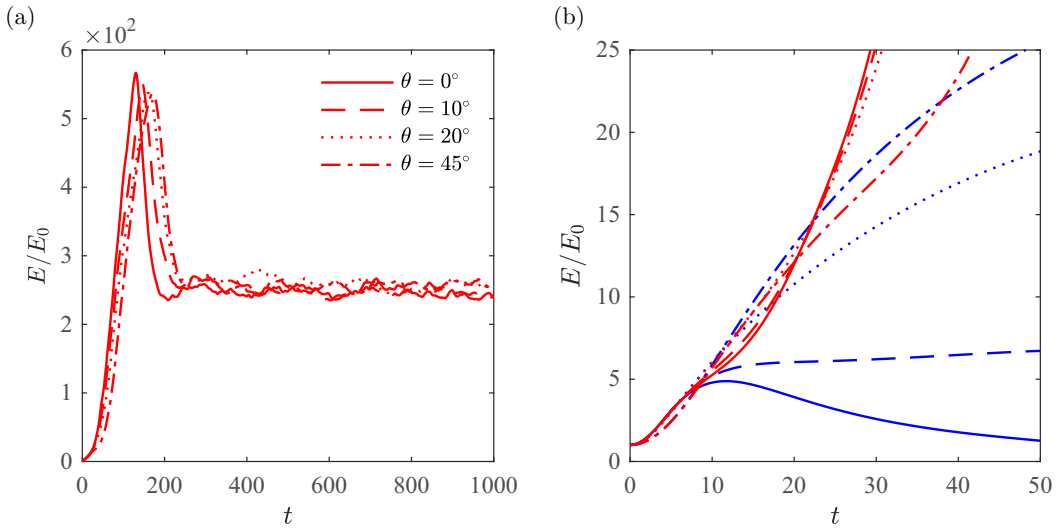

FIG. 8. Time evolution of (a) total perturbation kinetic energy for large-amplitude disturbance with $\theta = 0°, 10°, 20°, 45°$ and (b) comparison of kinetic energy evolution at initial times between large- (red) and small- (blue) amplitude perturbation.

D. Perturbation kinetic energy evolution

The perturbation kinetic energy evolution for the different initial orientations are plotted in Figs. 8(a) and 8(b). For $t < 10$ in Fig. 8(b), the large-amplitude perturbation for all θ has energy growth similar to the small-amplitude case. This initial time until $t \sim 10$ is the transient growth phase associated with the nonorthogonality of the eigenfunctions of the linear stability equations. Following this transient growth phase, viscous dissipation dominates for small-amplitude perturbation leading to decaying of kinetic energy.

For the large-amplitude disturbance, the nonlinearity is stronger, which further excites the perturbation energy [16]. In Fig. 8(b), the nonlinear excitation of energy could be clearly seen for the $\theta = 0°, 10°, 20°$ cases where the large-amplitude curves deviate significantly from their corresponding small-amplitude counterpart. For $\theta = 45°$, the energy growth of large-amplitude perturbation is not as rapid as for the other orientation angles. The energy is smaller than the small-amplitude case until $t \sim 40$, beyond which the curves rapidly separate. This also means that the transition time is delayed for the $\theta = 45°$ case.

The initial localized disturbance and its early evolution have energy in large scales [16]. Nonlinearity, however, transfers energy to higher harmonics and ultimately cascades energy through the entire wave-number range within the spots. These effects can be seen in the plots of the energy spectra in Figs. 9 and 10. These spectra elucidate the differences between the evolution of the $\theta = 0°$ and 45° cases during the early times. In Figs. 9(a) and 9(b), the evolution of streamwise averaged energy spectra of streamwise perturbation

$$\overline{E}_u(n_z) = \tfrac{1}{2}\langle \hat{u}'^2(x, y, n_z)\rangle_x \tag{13}$$

at the wall-model height $y = 0.25$ is plotted as a function of the spanwise integer wave number $[n_z = L_z/(2\pi/k_z)]$ for the $\theta = 0°$ and 45° cases. Here $\langle\cdot\rangle_x$ represents streamwise averaging, while u' is defined as the deviation from the horizontally averaged velocity. For $\theta = 0°$, the initial $u' = 0$ according to the initial condition (10) and therefore the energy spectrum is also 0. For the rotated initial condition $\theta = 45°$, the perturbation u' is finite and the corresponding energy spectral density is reported in the figure. While this initial difference is consequential at long times, it is nearly indiscernible at $t = 10$, where the energy spectral distributions appear similar for both the $\theta = 0°$

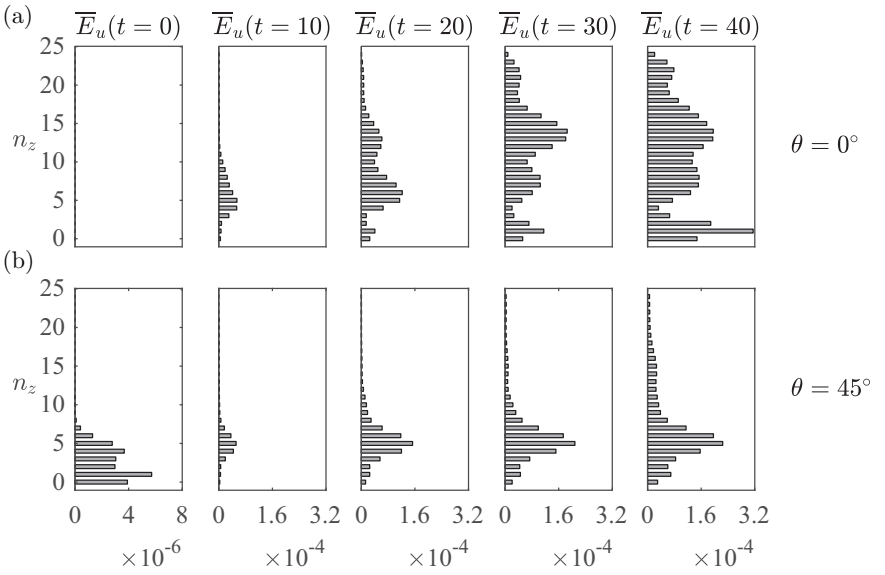

FIG. 9. Evolution of streamwise averaged streamwise energy spectra $[\overline{E}_u(n_z) = \frac{1}{2}\langle \hat{u}'^2(x, y = 0.25, n_z)\rangle_x]$ at $t = 0, 10, 20, 30, 40$ as a function of spanwise integer wave number $n_z = k_z L_z/2\pi$ for initial perturbation with (a) $\theta = 0^\circ$ and (b) $\theta = 45^\circ$.

and 45° cases. As time evolves, at $t = 20$, nonlinearity affects the $\theta = 0^\circ$ case. The energy spectrum peaks at higher wave numbers for $\theta = 0^\circ$, whereas there is only a single peak for $\theta = 45^\circ$. A similar scenario can be seen for times $t = 30, 40$ as well. For $\theta = 0^\circ$, the energy associated with $n_z = 0$ which represents the distortion to the base state increases rapidly. This is also an effect of nonlinearity. The spectral content for $n_z = 1$ also grows significantly as the spot occupies nearly half the spanwise extent of the domain at that time as shown in Fig. 11. In contrast, for $\theta = 45^\circ$, the energy growth for $n_z = 0, 1$ wave numbers is moderate, suggesting that the effect of nonlinearity is weaker at the reported times for this case. Based on the instantaneous fields (Fig. 11), this configuration has the smallest turbulent region at $t = 20$, which is consistent with such a delay in the broadening of the spectrum.

The early evolution of the spanwise averaged streamwise energy spectra

$$\overline{E}_u(n_x) = \tfrac{1}{2}\langle \hat{u}'^2(n_x, y, z)\rangle_z \tag{14}$$

for $\theta = 0^\circ, 45^\circ$ as a function of streamwise integer wave number $n_x = L_x/(2\pi/k_x)$ is plotted at the wall-model height $y = 0.25$ in Figs. 10(a) and 10(b). At $t = 10$, the energy spectra for both the $\theta = 0^\circ$ and 45° cases appear similar with only small differences. For subsequent times, the spectral content for smaller streamwise wave numbers grows and at $t = 40$ the spectra peak at $n_x = 1$ for both cases. The growth for $\theta = 0^\circ$ is more pronounced than for the $\theta = 45^\circ$ case. The energy associated with the base flow which corresponds to $n_x = 0$ also increases for both cases. The energy growth for the smaller streamwise wave number is consistent with the results from the linear stability analysis [16]. Physically, the energy concentration at small n_x represents the streamwise elongated structure of the perturbation. Together with the energy peaks at higher n_z observed earlier (they are due to nonlinearity) the spectra are consistent with streamwise elongated streaks with sharp spanwise gradients. These streaks are amplified further owing to a secondary instability mechanism and form the turbulent spot which undergoes a final breakdown to turbulence. We may conclude that LES with the WMSOM provides rich information regarding the large scales of this flow during transition even using a relatively coarse resolution.

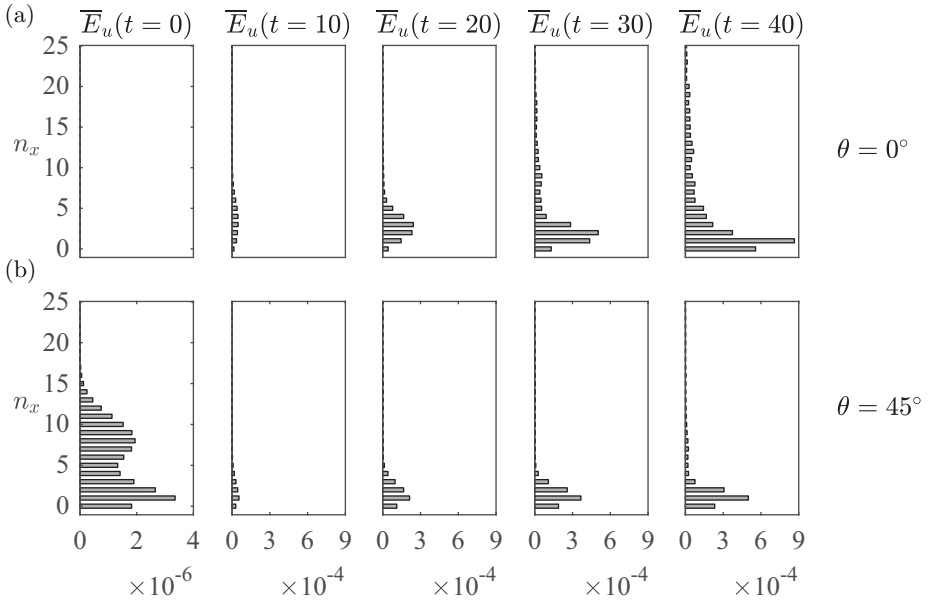

FIG. 10. Evolution of spanwise averaged streamwise energy spectra $[\overline{E}_u(n_x) = \frac{1}{2}\langle \hat{u}'^2(n_x, y = 0.25, z)\rangle_z]$ at $t = 0, 10, 20, 30, 40$ as a function of streamwise integer wave number $n_x = k_x L_x/2\pi$ for initial perturbation with (a) $\theta = 0°$ and (b) $\theta = 45°$.

V. RESULTS: SUBCRITICAL ORDERLY TRANSITION

In this section we consider LES of channel flow undergoing orderly transition, due to the interaction of discrete modes of the linear stability operator. We investigate transition by both K-type and H-type mechanisms. Details of the computational domain and grid parameters for the K-type transition simulations are summarized in Table IV. The results of K-type transition are discussed in Sec. V B and H-type transition in Sec. V C.

The transition is subcritical as the Reynolds number is $\mathrm{Re} = U_b h/\nu = 3333.33$ based on the bulk velocity U_b and the half-channel height h, which is less than the critical value $\mathrm{Re}_{\mathrm{cr}} = 3848$ [42]. The computational domain is shown in the schematic of Fig. 12. The streamwise (x) and spanwise (z) directions are periodic for all the simulations. A hyperbolic tangent stretched grid is used in the wall-normal direction for DNS and WRLES. For the WMLES and WMSOM, a uniform grid is

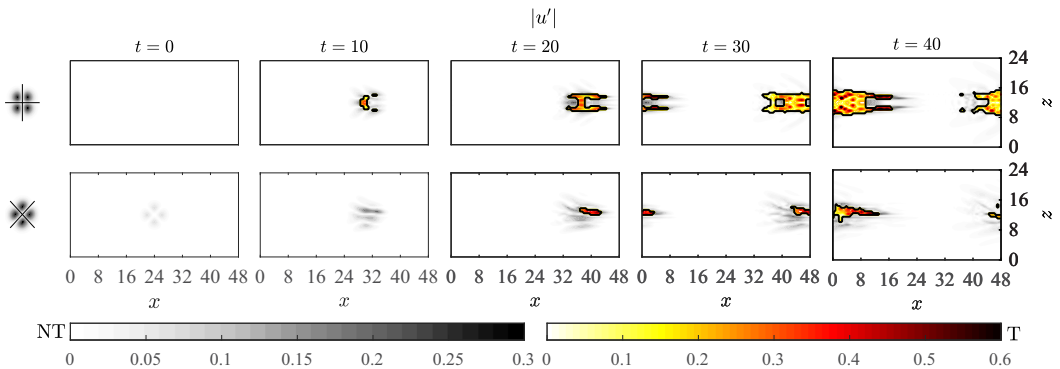

FIG. 11. Evolution of streamwise perturbation $|u'|$ at $t = 0, 10, 20, 30, 40$ for the $\theta = 0°, 45°$ cases.

TABLE IV. Computational domain size and grid points for LES and DNS of the K-type orderly transition.

Case	Re	Domain size $L_x \times L_y \times L_z$	No. of grid points $N_x \times N_y \times N_z$	Re_τ	Grid resolution $\Delta x^+ \times \Delta y^+_{\mathrm{min}} \times \Delta z^+$	y_{wm}
DNS	3333.33	$\frac{2\pi}{1.12} \times 2 \times \frac{2\pi}{2.1}$	$192 \times 192 \times 192$	206.33	$6.03 \times 0.1 \times 3.2$	
WRLES	3333.33	$\frac{2\pi}{1.12} \times 2 \times \frac{2\pi}{2.1}$	$64 \times 64 \times 64$	203.8	$18 \times 0.37 \times 17$	
WMLES/WMSOM	3333.33	$\frac{2\pi}{1.12} \times 2 \times \frac{2\pi}{2.1}$	$12 \times 28 \times 12$	197	$92 \times 14 \times 49$	0.18

used in the wall-normal coordinate. For WRLES, the no-slip boundary condition is used at the wall-normal boundaries $y = 0$ and $y = 2$. For the WMLES and WMSOM, $y = y_{\mathrm{wm}} = 0.18$ is chosen as the wall-model height, which corresponds to a wall-normal location $y^+_{\mathrm{wm}} = 36$ in inner units for the conditions once a fully turbulent state is achieved. As in the preceding section, for WMLES the wall stress from the equilibrium wall model (see Appendix A) is applied as the boundary condition everywhere on the top and bottom walls. For the WMSOM, based on the T/NT classification at the wall-model height, the no-slip condition is used in the nonturbulent regions and the wall stress from the equilibrium wall model is used in the turbulent regions.

A. Initial conditions

Following prior work [44], the initial condition consists of a Poiseuille base flow with 2D Tollmien-Schlichting (TS) waves and 3D oblique waves as perturbation components,

$$\boldsymbol{u}(\boldsymbol{x}, 0) = \tfrac{3}{2}[1 - (y-1)^2]\boldsymbol{e}_x + \mathrm{Re}\big[\epsilon_{2\mathrm{D}}\boldsymbol{u}_{2\mathrm{D}}(y)e^{ik_x x} + \tfrac{1}{2}\epsilon_{3\mathrm{D}}\boldsymbol{u}^+_{3\mathrm{D}}(y)e^{i[(k_x/s_x)x+(k_z/s_z)z+\phi]} + \tfrac{1}{2}\epsilon_{3\mathrm{D}}\boldsymbol{u}^-_{3\mathrm{D}}(y)e^{i[(k_x/s_x)x-(k_z/s_z)z+\phi]}\big], \tag{15}$$

where $\boldsymbol{u}_{2\mathrm{D}}(y)$ and $\boldsymbol{u}^{\pm}_{3\mathrm{D}}$ are the eigenmodes corresponding to 2D TS and 3D oblique waves, respectively, and $\boldsymbol{e}_x$ is the streamwise unit vector. These eigenmodes are obtained from the linear stability analysis using Orr-Sommerfeld and Squire equations [42].

A schematic of the base flow and perturbation profiles is shown in Fig. 12. The linear stability equations are solved for $k_x = 1.12$ and $k_z = \{0, 2.1\}$ wave numbers, which are equivalent to the experimental conditions in [45]. The fundamental wavelengths of the initial perturbations are $\lambda_x = 2\pi/1.12$ and $\lambda_z = 2\pi/2.1$. The domain size is then set to $L_x = s_x\lambda_x$ and $L_z = s_z\lambda_z$, where the integers s_x and s_z allow for subharmonic waves in the streamwise and spanwise directions. The parameter ϕ is the phase difference between the TS and oblique waves. In the present study, several initial conditions with different phases $\phi = \{0, 1, 2, 4, 6\}(\pi/8)$ are investigated. Table V lists the temporal eigenvalues [44] and amplitudes of the initial perturbations.

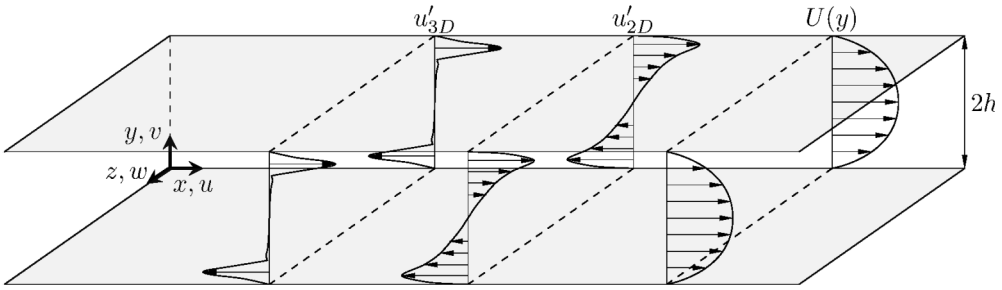

FIG. 12. Schematic of the flow configuration with the initial perturbation velocity profiles for the orderly transition.

TABLE V. Amplitude and growth rate of TS and oblique waves.

Wave type	$\mathrm{Re} = U_b h/\nu$	k_x	k_z	$\omega_r + i\omega_i$	Amplitude $(\epsilon_{2D}, \epsilon_{3D})$
TS	3333.33	1.12	0	$0.4733 - i0.0041$	0.045
Oblique	3333.33	1.12	2.1	$0.5455 - i0.1178$	$1.5 \times 10^{-3}, 6 \times 10^{-3}$

For the complex temporal eigenvalue ω in Table V, the corresponding eigenfunctions of the TS and oblique waves are plotted in Fig. 13. Each of the wall-normal profiles in the figure is normalized by the maximum value of $|\tilde{u}_{2D}(y)|$. The perturbation velocities are constructed such that the resultant amplitude of the TS wave component is $\epsilon_{2D} = 0.045$. For the oblique waves, two different amplitudes $\epsilon_{3D} = \{1.5, 6.0\} \times 10^{-3}$ are used. Starting with this initial velocity, the orderly transition mechanisms are investigated using DNS, WRLES, WMLES, and the WMSOM. The capability of the WMLES and WMSOM in predicting the different mechanisms of transition is investigated and the results are compared with DNS and WRLES.

B. Wall-modeled LES of fundamental K-type transition

The orderly transition with an oblique wave of amplitude $\epsilon_{3D} = 1.5 \times 10^{-3}$, $s_x = 1$, $s_z = 1$, and $\phi = 0$ is discussed. This oblique mode triggers fundamental K-type resonance. In Figs. 14(a)–14(c), the evolution of wall stress (τ_w) contours from the WRLES, WMLES, and WMSOM are plotted. In Fig. 14(d), the friction-Reynolds-number (Re_τ) time series from the different simulations are plotted together for comparison. The various times of the wall stress contours are marked in their respective Re_τ curves. The wall stress contours from the WMSOM are plotted with the T/NT interface obtained using the SOM. The grayscale colormap is used for the nonturbulent regions and the hot colormap for the turbulent regions. The Re_τ time evolution from WRLES shows excellent agreement with the DNS. The transition time is $t^* = 40$ for both WRLES and DNS and both yield a similar asymptotic $\mathrm{Re}_\tau \sim 200$ in the fully turbulent region at late times. Note that the horizontal resolution in this WRLES case is finer than that used in the preceding section for the bypass transition, possibly the reason for better agreement between WRLES and DNS.

Next we comment on the wall-modeled cases. From the τ_w contours [Fig. 14(b)] it is evident that the WMLES case does not undergo a transition to a turbulent state. From its initial condition $t = 0$, the wall stress for WMLES is too large and then decays as time evolves. The corresponding Re_τ curve [Fig. 14(d)] has a similar trend, where at $t = 0$, $\mathrm{Re}_\tau = 130$, while at large times it asymptotes

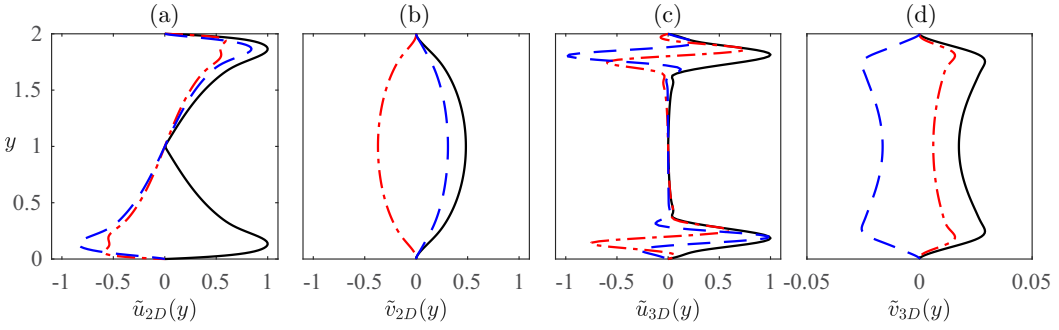

FIG. 13. Eigenfunction profiles at $\mathrm{Re} = 3333.33$ of (a) and (c) streamwise and (b) and (d) wall-normal components of Tollmien-Schlichting and oblique waves. The plots show the real (-·-·-), imaginary (– – –), and absolute (——) values of the eigenmodes.

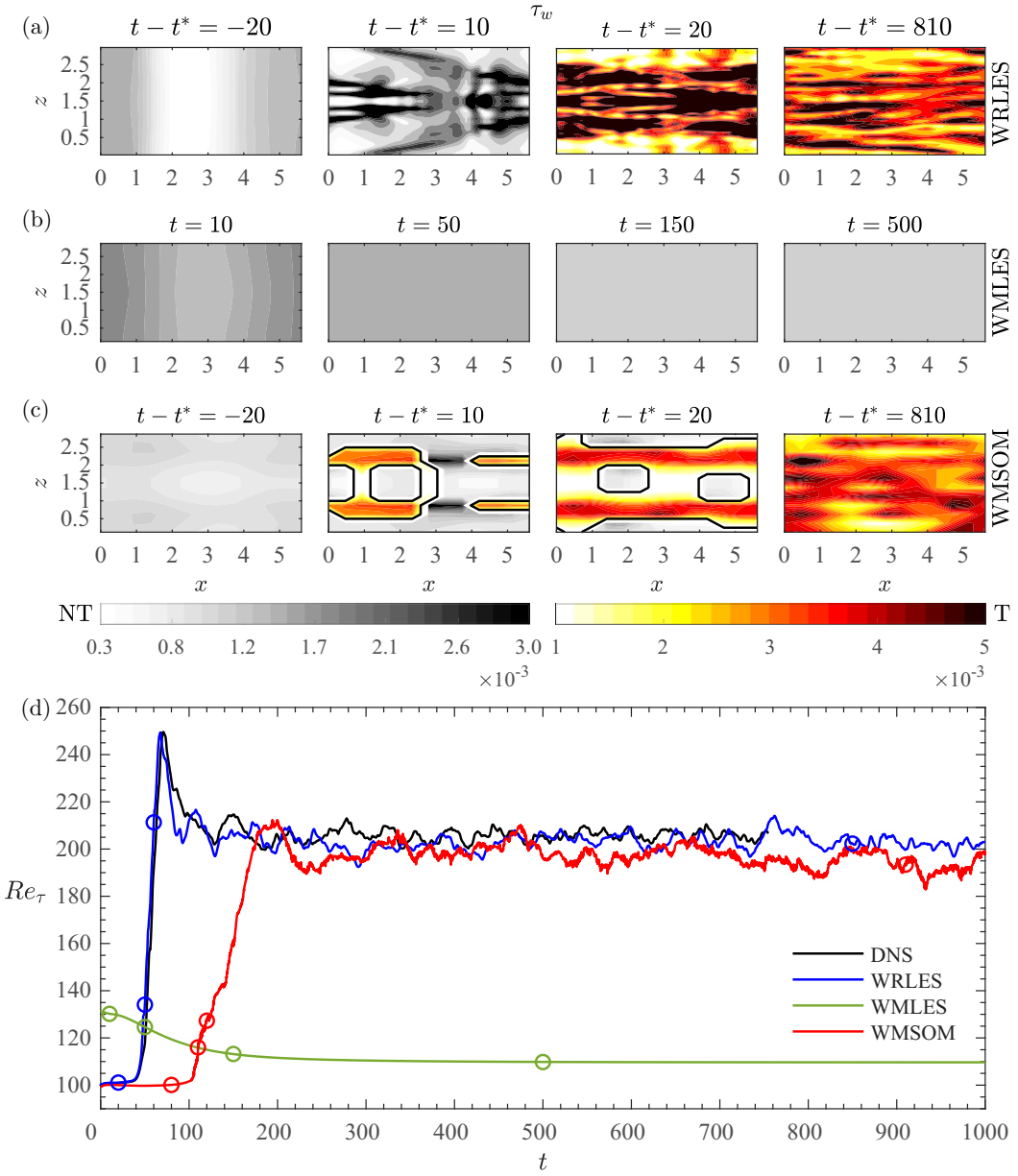

FIG. 14. Contours of wall stress τ_w at $y = 0$ from the (a) WRLES, (b) WMLES, and (c) WMSOM with the T/NT interface at different times. The transition times for the WRLES and WMSOM are $t^* = 40$ and 100, respectively. (d) Comparison of Re_τ evolution from the WRLES, WMLES, and WMSOM with that from the DNS. Circle markers correspond to the time at the which wall stress contours are plotted. Grayscale and hot colormaps represent nonturbulent and turbulent regions, respectively.

to a value of 110. The equilibrium wall model predicts a higher value for the stress, leading to Re_τ being higher than the $\mathrm{Re}_\tau = 100$ value corresponding to the viscous stress arising from the no-slip boundary condition in laminar flow.

In contrast, the SOM in the WMSOM identifies all the points as laminar before the transition time t^*, leading to $\mathrm{Re}_\tau = 100$ before the transition. For $t > t^*$, the WMSOM case undergoes transition

[Fig. 14(c)], as can be seen in both the contours and the Re_τ evolution. The Re_τ increases from 100 to a stationary state value of around 197, very close to the prediction from DNS. Before the transition at $t - t^* = -20$, the contour plots show that τ_w predicted in the WMSOM case is laminar. At a later time $t - t^* = 10$, which occurs after the transition, τ_w has both laminar and turbulent features. Later on at $t - t^* = 20$, the turbulent region has grown significantly. Time $t - t^* = 810$ corresponds to a fully turbulent state where the SOM identifies all the regions as turbulent. The fully turbulent τ_w contours at $t - t^* = 810$ from the WMSOM and WRLES are quite similar. The resulting $\mathrm{Re}_\tau \sim 197$ in the fully turbulent region is close to the value from DNS and WRLES, only about 4% lower. However, the transition time for the WMSOM is later than the DNS and WRLES cases, being delayed to $t^* \sim 100$.

In Fig. 15, we examine whether the performance of the WMSOM is robust to changes in the relative phase of the initial disturbances. We first draw attention to Fig. 15(b), where the friction Reynolds number is plotted versus time, for different phases $\phi = \{0, 1, 2, 4, 6\}\pi/8$. Note that WRLES for all phases undergoes transition at a time which is insensitive to the phase. In contrast, all the WMLES cases fail to transition to turbulence. In contrast, our WMSOM predicts a transition for all but one phase ($\phi = 2\pi/8$), although for the remaining phases the transition times vary. This trend is due to the low resolution of the initial condition in the WMSOM simulations. Contours of $|u'|$ are plotted for the transitional cases in Fig. 15(a). The turbulent (hot) and nonturbulent (grayscale) regions are identified using the SOM. At $t - t^* = -20$, all the different phases are laminar. The λ structure typical of the fundamental K-type orderly transition is clearly visible at this time. The contours for all the different phases at $t - t^* = 10$ show that the flow has undergone transition and the velocity field has features of both laminar and turbulent flow. The $|u'|$ at $t - t^* = 20$ shows that the region of turbulence has spread and grown bigger, which increases Re_τ. Turbulence continues to spread and fill the entire domain, leading to a fully turbulent state. The $|u'|$ at $t - t^* = 810$ are plotted from this fully turbulent state. Most of the regions in these contours are classified as turbulent by the SOM.

In order to document the effects of perturbation amplitude on the transition process, the amplitude of the oblique wave is increased to $\epsilon_{3D} = 6 \times 10^{-3}$ and the corresponding Re_τ is plotted in Fig. 16. For this ϵ_{3D}, the WMSOM of all the phases including $\phi = \pi/4$ (which did not undergo transition for $\epsilon_{3D} = 1.5 \times 10^{-3}$) also transitions to a fully turbulent state. Most of the phases undergo transition at the same time, earlier than the lower-amplitude perturbation cases, closer to the WRLES transition time, and reach a steady-state value $\mathrm{Re}_\tau \sim 200$ (the $\phi = \pi/4$ still transitions sometime later). Remarkably, even at this high-amplitude initial perturbation, the WMLES without T/NT classification does not undergo transition for any of the different phases. The evolution of Re_τ in WRLES for $\epsilon_{3D} = 6 \times 10^{-3}$ is similar to the $\epsilon_{3D} = 1.5 \times 10^{-3}$ case. Results are consistent with the anticipated impact of a coarse representation of the initial condition on the transition process.

C. H-type transition

In contrast to the K-type transition, in the H-type transition the λ structures ahead of the onset of turbulence have a staggered arrangement. In order to test the capacity of the WMSOM to reproduce the H-type transition, the initial disturbance (15) with the subharmonic $s_x = 2$, $s_z = 1$, $\phi = 0$, and $\epsilon_{3D} = 6 \times 10^{-3}$ is considered. The time evolution of such a perturbation is simulated in a domain of size $L_x = 2\lambda_x$ and $L_z = \lambda_z$, where $\lambda_x = 2\pi/1.12$ and $\lambda_z = 2\pi/2.1$ are the fundamental periodic length scales of the TS and oblique waves, respectively. To elucidate the differences between K- and H-type transitions, for the same domain size, the WMSOM of initial perturbation (15) with $s_x = 1$, $s_z = 1$, $\phi = 0$, and $\epsilon_{3D} = 6 \times 10^{-3}$ which undergo a K-type transition is also investigated.

In Figs. 17(a) and 17(b), snapshots of $|u'|$ at $y = 0.18$ and $t = 25, 200$ are shown as contour plots. Grayscale contours are used for laminar regions and a hot colormap is used for turbulent regions. Figure 17(a) corresponds to an initial perturbation with $s_x = 1$ and $s_z = 1$ and Fig. 17(b) is from an initial disturbance with $s_x = 2$ and $s_z = 1$. For better visualization of the arrangement of λ structures, since the spanwise direction is periodic, the snapshots in $0 \leqslant z \leqslant \lambda_z$ are copied to the

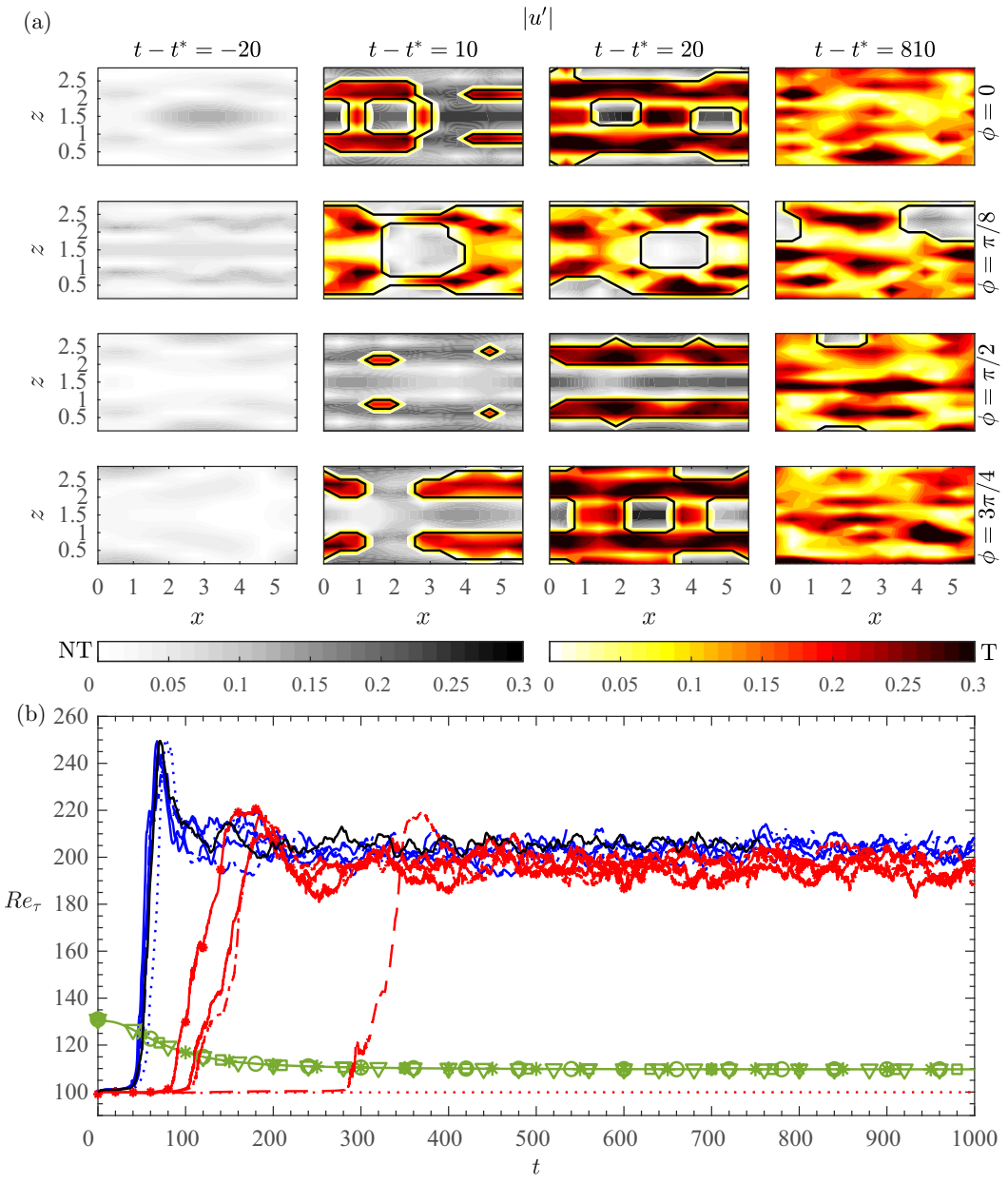

FIG. 15. (a) Contours of streamwise perturbation $|u'|$ from the WMSOM for different initial perturbations $\phi = 0, \pi/8, \pi/2, 3\pi/4$ at $y = 0.18$ and $t - t^* = -20, 10, 20, 810$ with $t^* = 100, 290, 100, 80$. (b) Plot of Re_τ time evolution from DNS (——) and WRLES for $\phi = 0$ (——), $\phi = \pi/8$ (– –), $\phi = \pi/4$ (·····), $\phi = \pi/2$ (–·–·), and $\phi = 3\pi/4$ (–*–); WMLES for $\phi = 0$ (——), $\phi = \pi/8$ (*), $\phi = \pi/4$ (○), $\phi = \pi/2$ (▽), and $\phi = 3\pi/4$ (□); and the WMSOM for $\phi = 0$ (——), $\phi = \pi/8$ (– –), $\phi = \pi/4$ (·····), $\phi = \pi/2$ (–·–·), and $\phi = 3\pi/4$ (–*–). Grayscale and hot colormaps represent nonturbulent and turbulent regions, respectively.

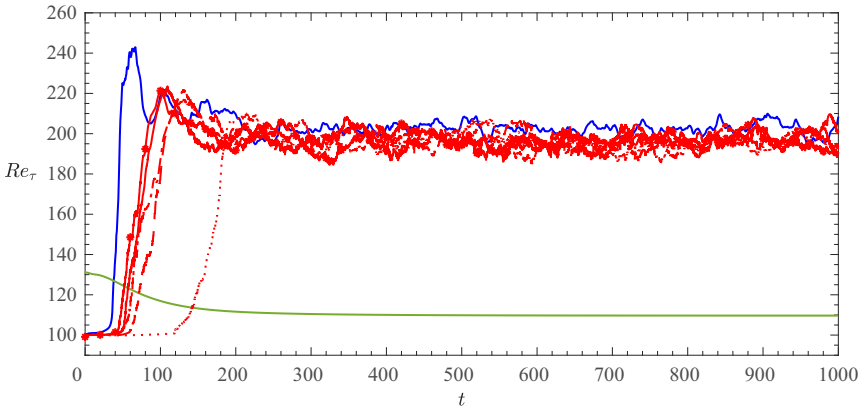

FIG. 16. Plot of Re_τ time evolution from WRLES for $\phi = 0$ (——), WMLES for $\phi = 0$ (——), and the WMSOM for $\phi = 0$ (——), $\phi = \pi/8$ (– –), $\phi = \pi/4$ (·····), $\phi = \pi/2$ (–·–·), and $\phi = 3\pi/4$ (–*–) of perturbation with $\epsilon_{3\mathrm{D}} = 6 \times 10^{-3}$.

region $\lambda_z < z < 2\lambda_z$. At $t = 25$, before transition, the $|u'|$ disturbance in Fig. 17(a) has successive rows of λ structures aligned, consistent with K-type transitions. In contrast, the corresponding plot in Fig. 17(b) shows $|u'|$ with a staggered arrangement of the λ structures which is typical of H-type transitions. Both cases undergo breakdown to a fully turbulent state, as seen from the contours at $t = 200$.

In Figs. 18(a) and 18(b), the spanwise averaged energy spectra of u' at $t = 25$ and $y = 0.18$ from both K- and H-type transitions are plotted as a function of the streamwise wave number $\kappa_x = k_x\lambda_x/2\pi$. For K-type transitions, there exists only one λ vortex within $x = \lambda_x$ [Fig. 17(a)]. The corresponding energy spectrum [Fig. 18(a)] has a peak at $\kappa_x = 1$ apart from the $\kappa_x = 0$ peak which

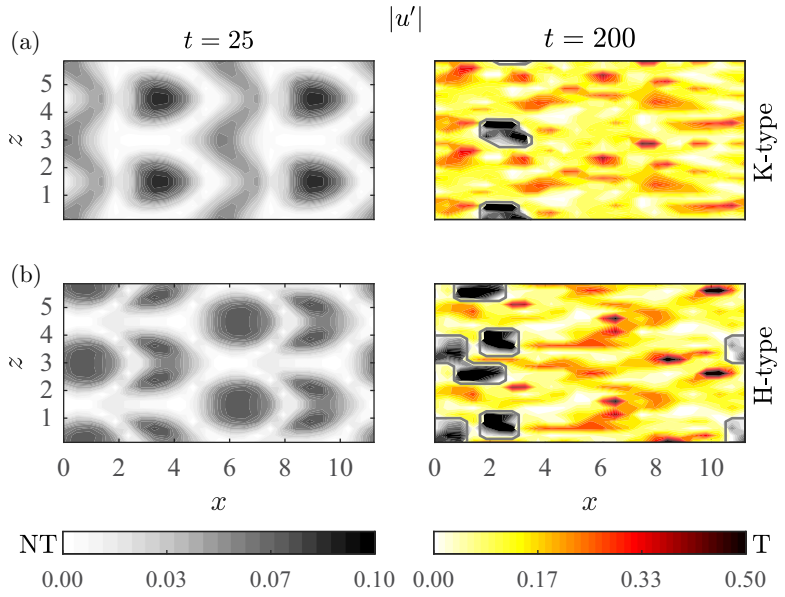

FIG. 17. Plot of $|u'|$ contours from the WMSOM ($\phi = 0, \epsilon_{3\mathrm{D}} = 6 \times 10^{-3}$) at $y = 0.18$ and $t = 25, 200$ showing (a) the K-type and (b) the H-type transition to turbulence.

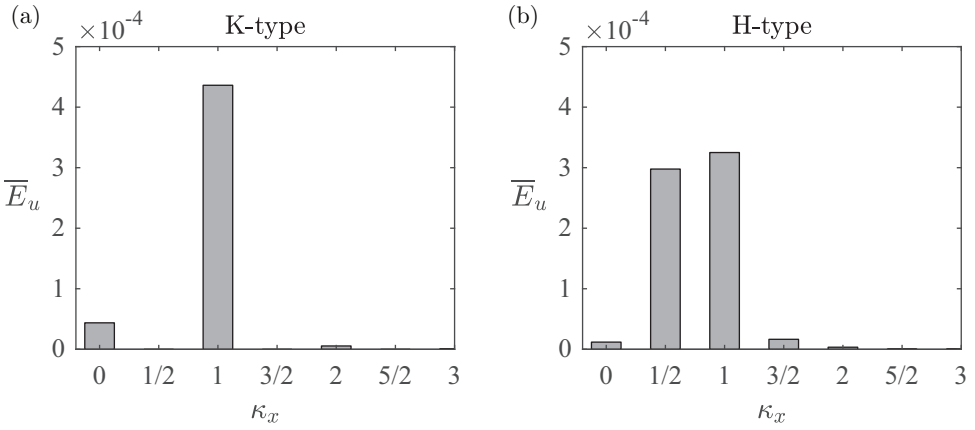

FIG. 18. Spanwise averaged streamwise energy spectra $[\overline{E}_u(k_x) = \frac{1}{2}\langle \hat{u}'(k_x, y, z)^2 \rangle_z]$ as a function of $\kappa_x = k_x \lambda_x / 2\pi$ at $y = 0.18$ and $t = 25$ showing (a) the K-type and (b) the H-type transition.

represents the base flow, whereas for the H-type transition only half of the λ structure is present within $x = \lambda_x$ [Fig. 17(b)]. In the corresponding energy spectrum [Fig. 18(b)], apart from the peaks at $\kappa_x = 0, 1$, there is an additional peak at $\kappa_x = \frac{1}{2}$ which is absent in the K-type spectral plot. Hence, these studies show that wall-modeled LES with SOM-based T/NT classification can simulate both the K- and H-type transition mechanisms.

VI. CONCLUSION

In this study, the potential of wall-modeled LES of the laminar-to-turbulence transition using T/NT classification based on a self-organizing map method was explored. The SOM method is an unsupervised-machine-learning classification technique that enables identifying laminar and turbulent regions without using arbitrary thresholds for the sensor. The ability of wall-modeled LES using the SOM to simulate both bypass and orderly transitions was tested.

For the bypass transition, when the disturbance amplitude is small, the SOM correctly identifies all the points in the domain as laminar. Similar to DNS, the perturbation undergoes an initial transient growth and subsequently decays due to viscous dissipation. For large initial perturbation amplitude, the WMLES and WMSOM both develop into a fully turbulent state. However, WMLES predicts a higher Re_τ in the laminar and transitional regimes than the corresponding DNS values, because the model does not distinguish between laminar and turbulent regions. Applying the wall-model only in the turbulent regions in the WMSOM predicts the correct Re_τ values in the laminar regime. Also, the transition time and the Re_τ growth in the transitional regime predicted by the WMSOM are comparable to DNS results.

In the case of the orderly transition, the wall-modeled LES without T/NT classification incorrectly predicts decay of the initial disturbances, whereas the WMSOM approach can predict both K- and H-type transitions. However, the transition time is delayed relative to DNS and wall-resolved LES. This mismatch in the transition time can be attributed to coarseness of the grid that barely enables capturing the amplitude of the applied perturbations. Increasing the amplitude of the oblique waves advances the transition time, leading to results that agree more closely with WRLES.

Some additional tests were performed extending the simulations that did not exhibit transition, i.e., WMLES cases without SOM T/NT classification and one case of the WMSOM of orderly transition with $\phi = \pi/4$ and $\epsilon_{3D} = 1.5 \times 10^{-3}$, to very long times. It was observed that these cases could eventually become turbulent but at much later times than DNS or WRLES, after the prescribed initial perturbation energy had decayed many orders of magnitude. It could be concluded that these

belated transition events occurred in response to numerical effects that eventually come to the fore, rather than representing a physically realistic evolution of the initially imposed perturbations.

One of the most important advantages of wall-modeled LES (including the SOM T/NT classification) is reduced computational cost. The wall-clock time C_{time} taken to compute one domain flowthrough advection time unit using a single processor was measured for the DNS, WRLES, and WMSOM of both orderly and bypass transition cases. For the former, the ratio of the wall-clock time required for the WMSOM compared to WRLES is 0.0027, whereas the ratio of the wall-clock time required for DNS compared to WRLES is 94. Similarly, for bypass transition, the wall-clock time ratios for the WMSOM and DNS with respect to WRLES are 0.0039 and 71, respectively. Now consider a grid with $N_x \times N_y \times N_z$ points and let us assume that it takes N_t time steps to simulate one convective time unit. The total operation count C_{tot} for computing tridiagonal inversions and fast Fourier transforms in the pressure Poisson equation of the fractional-step algorithm can be estimated as $C_{\text{tot}} \sim O(N_t N_x N_y N_z[\log(N_x) + \log(N_z) + 10])$. The ratios obtained using this estimate for total operation counts for the various $N_t N_x N_y N_z$ values in the different runs are consistent with the empirically measured wall-clock time ratios mentioned above. The analysis thus shows that the WMSOM is computationally much more efficient than WRLES (by about a factor of 300 in our simulations) and of course even more so compared to DNS (by about a factor of 25 000), providing a practical tool to simulate the laminar-turbulent transition process. Follow-up work could examine the performance of the WMSOM when relaminarization occurs and consider inclusion of additional effects such as expansion/contraction, curvature, rotation, and roughness.

ACKNOWLEDGMENTS

This research was supported by the Office of Naval Research (Grant No. N00014-17-1-2937). Computational resources were provided by Maryland Advanced Research Computing Center. Discussions with Dr. Zhao Wu and Mengze Wang are greatly appreciated.

APPENDIX A: EXPLICITLY FITTED EQUILIBRIUM WALL MODEL

The wall stress for the turbulent regions of the transitional flow is obtained using a recently developed version of the equilibrium wall model [46]. The model assumes the flow is fully turbulent and in near-wall equilibrium conditions. It has been derived by solving the Reynolds-averaged Navier-Stokes (RANS) equations neglecting the unsteady and acceleration terms and using a standard mixing length model with a van Driest damping function to smoothly merge the viscous and logarithmic-layer regions. The outcome of the numerical integration was cast in terms of two Reynolds numbers, the known grid-velocity Reynolds number Re_Δ and the unknown grid-friction velocity Reynolds number $\text{Re}_{\tau\Delta}$. These are defined according to

$$\text{Re}_\Delta = \frac{U_s y_{\text{wm}}}{\nu}, \quad \text{Re}_{\tau\Delta} = \frac{u_\tau y_{\text{wm}}}{\nu}, \tag{A1}$$

respectively, where $U_s = \sqrt{\tilde{u}^2 + \tilde{w}^2}$ is the local streamwise velocity available in LES at the grid point at a distance y_{wm} from the wall.

The numerical results obtained in Ref. [46] are shown in Fig. 19 by plotting the resulting Re_Δ on the x axis and $\text{Re}_{\tau\Delta}$ on the y axis. The numerical results for $\text{Re}_{\tau\Delta}$ as a function of a given Re_Δ smoothly transition from the viscous sublayer to the logarithmic layer. At small Reynolds numbers, the expected trend is $\text{Re}_{\tau\Delta} \sim \text{Re}_\Delta^{1/2}$ (when y_{wm} is in the viscous region), whereas at high Re_Δ the behavior is a slow approach to linear with subleading logarithmic corrections. In order to fit this numerical result Ref. [46] noted that the function $\text{Re}_{\tau\Delta}(\text{Re}_\Delta)$ should transition between a $1/2$ power law at low Re_Δ towards a power law with exponent $\beta_1 \sim 0.9$ at high Re_Δ. The following transition function was proposed, with a transition sharpness controlled by parameter β_2:

$$\text{Re}_{\tau\Delta}^{\text{fit}}(\text{Re}_\Delta) = \kappa_4 \text{Re}_\Delta^{\beta_1}[1 + (\kappa_3 \text{Re}_\Delta)^{-\beta_2}]^{(\beta_1 - 1/2)/\beta_2}. \tag{A2}$$

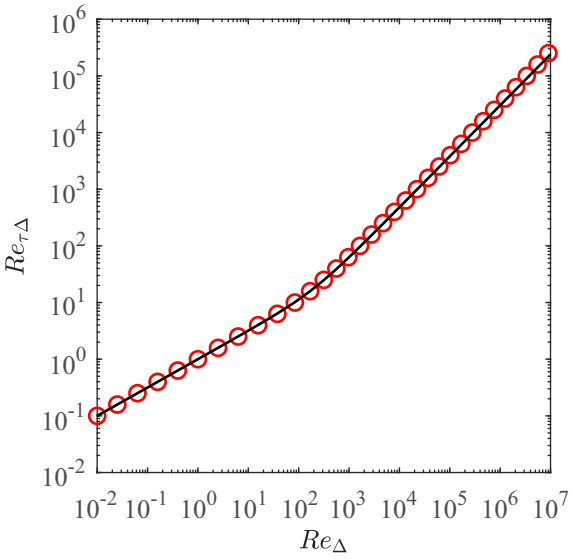

FIG. 19. Red circles depict the numerical solution of the mixing-length RANS equations over a wide range of Re_Δ [46]. The dark solid line shows the empirical fit given by Eq. (A2).

Choosing constant values $\beta_1 = 0.9$, $\beta_2 = 1.2$, $\kappa_3 = 0.005$, and $\kappa_4 = \kappa_3^{\beta_1 - 1/2}$ gives results with very small errors for the range of Re_Δ values in this study.

The wall model then consists of using the local LES velocity U_s at $y = y_{\mathrm{wm}}$ to evaluate Re_Δ, evaluating Eq. (A2) to determine $\mathrm{Re}_{\tau\Delta}$ locally, then determining the friction velocity according to $u_\tau = \nu\,\mathrm{Re}_{\tau\Delta}/y_{\mathrm{wm}}$, and finally determining the wall stress ($\tilde{\tau}_w$) and its components $\tilde{\tau}_{xy,w}$ and $\tilde{\tau}_{yz,w}$ for the turbulent regions according to

$$\tilde{\tau}_w = u_\tau^2 = \left(\frac{\mathrm{Re}_{\tau\Delta}}{\mathrm{Re}_\Delta}\right)^2 U_s^2, \tag{A3}$$

$$\tilde{\tau}_{xy,w} = \frac{\tilde{u}(x, y_{\mathrm{wm}}, z)}{U_s(x, y_{\mathrm{wm}}, z)}\tilde{\tau}_w, \tag{A4}$$

$$\tilde{\tau}_{yz,w} = \frac{\tilde{w}(x, y_{\mathrm{wm}}, z)}{U_s(x, y_{\mathrm{wm}}, z)}\tilde{\tau}_w. \tag{A5}$$

APPENDIX B: CONDITIONALLY AVERAGED DYNAMIC SGS MODEL WITH NONDYNAMIC SCALE DEPENDENCE

For WRLES and WMLES, the model coefficient C_s^2 in the expression for eddy viscosity (7) is computed through the well-known plane-averaged dynamic procedure [21]

$$C_s^2 = \frac{\langle M_{ij} L_{ij}^d \rangle}{\langle M_{kl} M_{kl} \rangle}, \tag{B1}$$

where $\langle\cdot\rangle$ represents planar x-z averaging, $L_{ij} = \widetilde{\tilde{u}_i \tilde{u}_j} - \tilde{\bar{u}}_i \tilde{\bar{u}}_j$, $L_{ij}^d = L_{ij} - \frac{1}{3} L_{kk}\delta_{ij}$, $M_{ij} = 2\,\tilde{\Delta}^2 \widetilde{|\tilde{S}|\tilde{S}}_{ij} - 2\,\beta|\tilde{\bar{S}}|\tilde{\bar{S}}_{ij}$, and $\beta = C_s^2(\tilde{\bar{\Delta}})/C_s^2(\tilde{\Delta})$ is a scale-dependent correction factor [36]. The overline represents test filtering and the corresponding test-filter length scale is $\tilde{\bar{\Delta}} = (2\Delta x \Delta y 2\Delta z)^{1/3}$. The ratio of model coefficients, β, at two scales depends on whether one is applying WRLES or WMLES. For the WRLES, a scale-independent dynamic Smagorinsky SGS model (i.e., with $\beta = 1$) can be used since in WRLES the grid resolution near the wall is typically

much finer than the local integral scale of turbulence. The planar averaging in Eq. (B1) is done considering the entire x-z plane.

For WMLES, a scale-dependent dynamic SGS model [36] must be used since the near-wall resolution (the distance to the wall) is very similar to the local integral scale of turbulence, where the assumption of scale-invariance breaks down. In order to avoid incurring additional computational cost involved in additional test filtering as used in Refs. [36,47], here we use a nondynamic version of the scale-dependent model and β is modeled as the ratio of the Mason wall-damping function [48] evaluated at two scales, i.e.,

$$\beta = \frac{C_s^2(\bar{\tilde{\Delta}})}{C_s^2(\tilde{\Delta})} = \frac{l_d^2(\bar{\tilde{\Delta}})}{l_d^2(\tilde{\Delta})}, \tag{B2}$$

where

$$l_d^2(\Delta) = \left[1 + \left(\frac{\kappa y}{C_0 \Delta}\right)^{-2}\right]^{-1},$$

with $\kappa = 0.41$ (von Kármán constant), $C_0 = 0.16$, and $\Delta = \tilde{\Delta}$ or $\bar{\tilde{\Delta}}$.

For the scale-dependent dynamic SGS model used in the WMSOM, a conditional planar averaging is done in the dynamic procedure in Eq. (B1). At each wall-normal plane, the planar averaging is done only considering the turbulent regions of the flow, i.e., we compute

$$C_s^2(y) = \frac{\langle M_{ij} L_{ij}^d | y, T \rangle}{\langle M_{kl} M_{kl} | y, T \rangle}, \tag{B3}$$

where the condition T is met at all points in the flow at a given height y when $\boldsymbol{a} \cdot \boldsymbol{X} + 1 < 0$ (see Sec. II). In the nonturbulent regions, the eddy viscosity is switched off by setting it to zero.

[1] H. P. Hodson and R. J. Howell, Bladerow interactions, transition, and high-lift aerofoils in low-pressure turbines, Annu. Rev. Fluid Mech. **37**, 71 (2005).

[2] L. Kleiser and T. A. Zang, Numerical simulation of transition in wall-bounded shear flows, Annu. Rev. Fluid Mech. **23**, 495 (1991).

[3] T. A. Zaki, From streaks to spots and on to turbulence: Exploring the dynamics of boundary layer transition, Flow Turbul. Combust. **91**, 451 (2013).

[4] P. A. Durbin, Perspectives on the phenomenology and modeling of boundary layer transition, Flow Turbul. Combust. **99**, 1 (2017).

[5] P. S. Klebanoff, K. D. Tidstrom, and L. M. Sargent, The three-dimensional nature of boundary-layer instability, J. Fluid Mech. **12**, 1 (1962).

[6] T. Herbert, Secondary instability of boundary layers, Annu. Rev. Fluid Mech. **20**, 487 (1988).

[7] M. V. Morkovin, in *Instabilities and Turbulence in Engineering Flows*, edited by D. E. Ashpis, T. B. Gatski, and R. Hirsh, Fluid Mechanics and Its Applications, Vol. 16 (Springer, Dordrecht, 1993), pp. 3–30.

[8] G. I. Taylor, in *Proceedings of the Fifth International Congress for Applied Mechanics, Cambridge, 1938* (Wiley, New York, 1939), pp. 294–310.

[9] O. M. Phillips, Shear-flow turbulence, Annu. Rev. Fluid Mech **1**, 245 (1969).

[10] P. Andersson, L. Brandt, A. Bottaro, and D. Henningson, On the breakdown of boundary layer streaks, J. Fluid Mech. **428**, 29 (2001).

[11] N. Vaughan and T. Zaki, Stability of zero-pressure-gradient boundary layer distorted by unsteady Klebanoff streaks, J. Fluid Mech. **681**, 116 (2011).

[12] K. P. Nolan and T. A. Zaki, Conditional sampling of transitional boundary layers in pressure gradients, J. Fluid Mech. **728**, 306 (2013).

[13] M. J. P. Hack and T. A. Zaki, Streak instabilities in boundary layers beneath free-stream turbulence, J. Fluid Mech. **741**, 280 (2014).
[14] N. D. Sandham and L. Kleiser, The late stages of transition to turbulence in channel flow, J. Fluid Mech. **245**, 319 (1992).
[15] N. Gilbert and L. Kleiser, in *Near-Wall Turbulence: 1988 Zoran Zaric Memorial Conference*, Dubrovnik, 1988, edited by S. J. Kline and N. H. Afgan, Proceedings of the International Centre for Heat and Mass Transfer, Vol. 28 (Hemisphere, London, 1989).
[16] D. S. Henningson, A. Lundbladh, and A. V. Johansson, A mechanism for bypass transition from localized disturbances in wall-bounded shear flows, J. Fluid Mech. **250**, 169 (1993).
[17] D. R. Chapman, Computational aerodynamics development and outlook, AIAA J. **17**, 1293 (1979).
[18] H. Choi and P. Moin, Grid-point requirements for large eddy simulation: Chapman's estimates revisited, Phys. Fluids **24**, 011702 (2012).
[19] U. Piomelli and T. A. Zang, Large-eddy simulation of transitional channel flow, Comput. Phys. Commun. **65**, 224 (1991).
[20] U. Piomelli, T. A. Zang, C. G. Speziale, and M. Y. Hussaini, On the large-eddy simulation of transitional wall bounded flows, Phys. Fluids A **2**, 257 (1990).
[21] M. Germano, U. Piomelli, P. Moin, and W. H. Cabot, A dynamic subgrid-scale eddy viscosity model, Phys. Fluids A **3**, 1760 (1991).
[22] U. Piomelli and E. Balaras, Wall-layer models for large-eddy simulations, Annu. Rev. Fluid Mech. **34**, 349 (2002).
[23] S. Kawai and J. Larsson, Wall-modeling in large eddy simulation: Length scales, grid resolution, and accuracy, Phys. Fluids **24**, 015105 (2012).
[24] T. Sayadi and P. Moin, Large eddy simulation of controlled transition to turbulence, Phys. Fluids **24**, 114103 (2012).
[25] P. R. Voke and Z. Yang, Numerical study of bypass transition, Phys. Fluids **7**, 2256 (1995).
[26] P. R. Voke, Subgrid-scale modelling at low mesh Reynolds number, Theor. Comput. Fluid Dyn. **8**, 131 (1996).
[27] J. W. Deardorff, A numerical study of three-dimensional turbulent channel flow at large Reynolds numbers, J. Fluid Mech. **41**, 453 (1970).
[28] J. Bodart and J. Larsson, *Center for Turbulence Research Annual Research Briefs 2012* (Stanford University, Stanford, 2012).
[29] S. L. Brunton, B. R. Noack, and P. Koumoutsakos, Machine learning for fluid mechanics, Annu. Rev. Fluid Mech. **52**, 477 (2020).
[30] Z. Wu, J. Lee, C. Meneveau, and T. Zaki, Application of a self-organizing map to identify the turbulent-boundary-layer interface in a transitional flow, Phys. Rev. Fluids **4**, 023902 (2019).
[31] Z. Wu, T. A. Zaki, and C. Meneveau, High-Reynolds-number fractal signature of nascent turbulence during transition, Proc. Natl. Acad. Sci. U.S.A. **117**, 3461 (2020).
[32] http://turbulence.pha.jhu.edu/.
[33] R. C. Gonzalez and R. E. Woods, *Digital Image Processing* (Prentice Hall, Upper Saddle River, 2008).
[34] P. Moin, K. Squires, W. Cabot, and S. Lee, A dynamic subgrid-scale model for compressible turbulence and scalar transport, Phys. Fluids A **3**, 2746 (1991).
[35] D. K. Lilly, A proposed modification of the Germano subgrid-scale closure method, Phys. Fluids A **4**, 633 (1992).
[36] F. Porté-Agel, C. Meneveau, and M. B. Parlange, A scale-dependent dynamic model for large-eddy simulation: Application to a neutral atmospheric boundary layer, J. Fluid Mech. **415**, 261 (2000).
[37] A. Agarwal, L. Brandt, and T. Zaki, Linear and nonlinear evolution of a localized disturbance in polymeric channel flow, J. Fluid Mech. **760**, 278 (2014).
[38] S. J. Lee and T. A. Zaki, Simulations of natural transition in viscoelastic channel flow, J. Fluid Mech. **820**, 232 (2017).
[39] M. Rosenfeld, D. Kwak, and M. Vinokur, A fractional step solution method for the unsteady incompressible Navier-Stokes equations in generalized coordinate systems, J. Comput. Phys. **94**, 102 (1991).

[40] M. T. Landahl, in *Proceedings of the Eighth Biennial Symposium on Turbulence, University of Missouri-Rolla, 1983*, edited by X. B. Reed (University of Missouri-Rolla, Rolla, 1984).
[41] K. S. Breuer and J. H. Haritonidis, The evolution of a localized disturbance in a laminar boundary layer. Part 1. Weak disturbances, J. Fluid Mech. **220**, 569 (1990).
[42] P. J. Schmid and D. S. Henningson, *Stability and Transition in Shear Flows*, Applied Mathematical Sciences, Vol. 142 (Springer, New York, 2001).
[43] O. Marxen and T. A. Zaki, Turbulence in intermittent transitional boundary layers and in turbulence spots, J. Fluid Mech. **860**, 350 (2019).
[44] T. Zang, N. Gilbert, and L. Kleiser, in *Instability and Transition*, edited by M. Y. Hussaini and R. G. Voigt, ICASE/NASA LaRC Series (Springer, New York, 1990), pp. 283–299.
[45] M. Nishioka, S. I. A, and Y. Ichikawa, An experimental investigation of the stability of plane Poiseuille flow, J. Fluid Mech. **72**, 731 (1975).
[46] C. Meneveau, A note on fitting a generalised moody diagram for wall modelled large-eddy simulations, J. Turbul. **21**, 650 (2020).
[47] E. Bou-Zeid, C. Meneveau, and M. Parlange, A scale-dependent Lagrangian dynamic model for large eddy simulation of complex turbulent flows, Phys. Fluids **17**, 025105 (2005).
[48] P. J. Mason and D. J. Thomson, Stochastic backscatter in large-eddy simulations of boundary layers, J. Fluid Mech. **242**, 51 (1992).